



Role of convecting disturbances and acoustic standing waves in supersonic impinging jet

MyungJun Song o, Serdar Seçkin o and Farrukh S. Alvi

¹Florida Center for Advanced Aero-Propulsion, Department of Mechanical Engineering, Florida A&M University and Florida State University (FAMU-FSU) College of Engineering, Tallahassee, FL 32310, USA

Corresponding author: MyungJun Song, msong@fsu.edu

(Received 4 February 2025; revised 6 August 2025; accepted 2 September 2025)

Supersonic jets impinging on a ground plane produce a highly unsteady jet shear layer, often resulting in extremely high noise level. The widely accepted mechanism for this jet resonance involves a feedback loop consisting of downstream-travelling coherent structures and upstream-propagating acoustic waves. Despite the importance of coherent structures, often referred to as disturbances, that travel downstream, a comprehensive discussion on the disturbance convection velocity has been limited due to the challenges posed by non-intrusive measurement requirements. To determine the convection velocity of disturbances in the jet shear layer, a high-speed schlieren flow visualisation is carried out, and phase-averaged wave diagrams are constructed from the image sets. The experiments are conducted using a Mach 1.5 jet under various nozzle pressure ratios and across a range of impingement distances. A parametric analysis is performed to examine the influence of nozzle pressure ratio on the convection velocity and phase lead/lag at specific impingement distances. The results reveal that impingement tonal frequency is nearly independent of the disturbance convection velocity, except in cases of staging behaviour. They also demonstrated that slower downstream convection velocity of the disturbance corresponds to larger coherent structures, resulting in increased noise levels. Based on the observation of acoustic standing waves, an acoustic speed-based frequency model has been proposed. With the help of the allowable frequency range calculated from the vortex-sheet model, this model can provide a good approximation for the majority of axisymmetric impingement tonal frequencies.

Key words: jet noise, acoustics, aeroacoustics

1. Introduction

Supersonic impinging jets tend to experience strong shear-layer instabilities that ultimately lead to resonance, which is accompanied by high noise levels and structural vibrations. In short takeoff vertical landing (STOVL) applications, these vibrations can cause structural fatigue (Alvi *et al.* 2003) and aggravate entrainment resulting in a higher suckdown force and lift loss due to negative pressure below the fuselage (Wyatt 1958; Alvi *et al.* 2003). Thereby, a better understanding of the impingement jet flowfields is essential for the design of efficient STOVL aircraft.

A schematic of a single impinging jet flowfield, accompanied by an instantaneous schlieren image on the left-hand side, is presented in figure 1. Here, the jet impinges upon the ground plate, resulting in the formation of a radial wall jet. An in-depth examination of the shock structures can be found in the work of Alvi, Ladd & Bower (2002). Under certain conditions, the impinging jet undergoes resonance, leading to the formation of highly unsteady flow features. For example, large-scale coherent structures become prominent within the jet shear layer as they convect downstream. Upon impingement on the ground plane, these coherent structures generate acoustic waves. The jet resonance mechanism is generally understood as a feedback loop, which consists of downstreamconvecting large-scale coherent structures and upstream-propagating acoustic waves that excite shear-layer instabilities (Powell 1988). Furthermore, there has been growing interest in the vortex-sheet model (Tam & Hu 1989; Tam & Ahuja 1990) for the study of screech and impingement tones. This model proposes that intrinsic, upstreampropagating neutral waves are involved in the feedback mechanism. This approach has advanced the understanding of resonating free jets (Towne et al. 2017; Edgington-Mitchell et al. 2022; Nogueira et al. 2024). For instance, Jaunet et al. (2019) demonstrated that the extinction of impingement tones corresponds to the dispersion relation of the vortex-sheet model. Extensive analysis of upstream-propagating acoustic waves using the vortex-sheet model has also been conducted based on large-eddy simulation data (Bogey & Gojon 2017), offering detailed insights into the underlying wave dynamics. Comprehensive details of resonance characteristics in screeching and impinging jets are well documented by Edgington-Mitchell (2019). Recent advancements in modern datadriven techniques – such as proper orthogonal decomposition (POD) (Chatterjee 2000), dynamic mode decomposition (DMD) (Schmid 2010) and spectral POD (SPOD) (Towne, Schmidt & Colonius 2018; Schmidt & Colonius 2020) – have significantly deepened our understanding of turbulent supersonic jet instabilities (Jordan & Colonius 2013; Sinha et al. 2014; Schmidt et al. 2018). In impinging jet configurations, Edgington-Mitchell et al. (2018) employed the POD technique to demonstrate that the closure of the feedback loop is completed by upstream-travelling acoustic waves rather than hydrodynamic perturbations. For dual impinging jets, the use of POD and DMD techniques successfully revealed interactions between the two jets (Song et al. 2021, 2022b). Moreover, the application of SPOD to high-fidelity large-eddy simulation data has successfully extracted dominant modes, effectively capturing the key dynamics responsible for impinging jet resonance (Karami & Soria 2018; Fiore et al. 2022).

As is widely accepted, the feedback loop of impinging jet resonance can be expressed by Powell's formulation (Powell 1988) as follows:

$$\frac{N+P}{f_{impinging}} = \frac{H}{C_a} + \int_0^H \frac{\mathrm{d}x}{C_{st}} \quad (N=1, 2, 3, \dots),$$
 (1.1)

where H is the distance between the impingement plate and the nozzle exit plane and C_a represents the ambient acoustic wave velocity; C_{st} denotes the convection velocity of

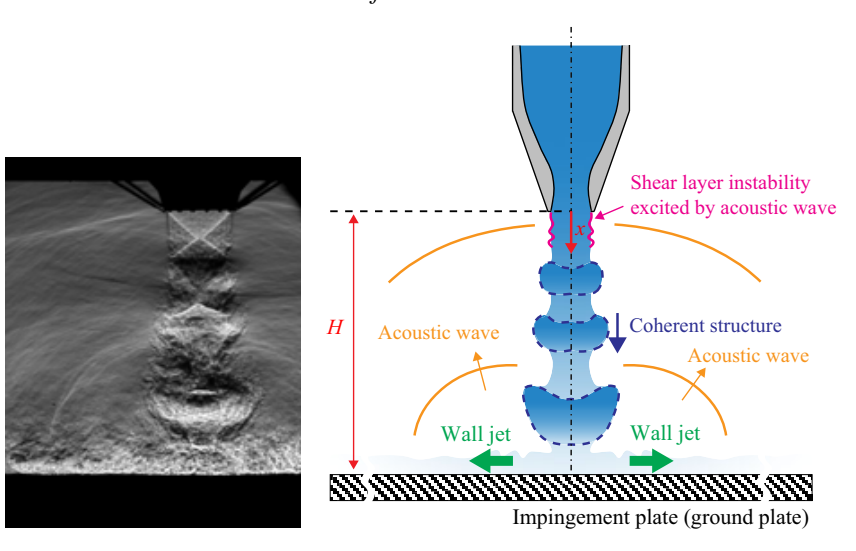


Figure 1. Schematic of impinging jet flowfield with axisymmetric disturbance/shear-layer structures (not to scale).

disturbances along the jet shear layer as a function of x, indicating that the convection velocity of large-scale coherent structures varies as they convect. The first and second terms on the right-hand side of (1.1) represent the travel times for the acoustic waves and coherent structures to traverse the impingement distance (H), respectively. Thus, the right-hand side of (1.1) corresponds to the loop period ($T_{loop,sl}$). Term $f_{impinging}$ denotes the frequency of the impingement tone and N+P is the number of cycles of T_{period} $(=1/f_{impinging})$ generated within the loop period $(T_{loop,st})$, where N is an integer and P represents a phase lead/lag (-1 < P < 1). Equation (1.1) implies that the disturbance convection velocity plays a primary role in determining the impingement tonal frequency, as it contributes to the time scale for half the path of the feedback loop. A prior experiment (Powell 1988) has shown that the impingement tonal frequency at certain impingement distances is almost independent of the nozzle pressure ratio (NPR), except in cases involving the staging behaviour of impingement tones. A previous study (Krothapalli et al. 1999) has shown that a higher NPR leads to an increase in the disturbance convection velocities. The disturbance convection velocity is one of the important factors that affect the impingement frequency, as indicated by (1.1). Hence, the influence of NPR, a primary operating parameter, on the disturbance convection velocity and its consequent effect on the impingement tonal frequency remain ambiguous.

In addition, it has been demonstrated that the disturbance convection velocity varies with changes in impingement distance (Krothapalli *et al.* 1999). Therefore, when employing (1.1) to predict or validate impingement tonal frequency across various impingement distances, using the mean convection velocity and phase lead/lag requires a cautious approach. However, there is a lack of disturbance convection velocity data in the literature. Consequently, it often becomes necessary to assume a constant mean convection velocity and phase lead/lag across different impingement distances. While adjustments to the phase lead/lag values can yield acceptable agreement with experimental data over a range of impingement distances, a more comprehensive analysis is required for a deeper understanding of how impingement distance affects the flowfield. This is not to imply deficiencies in Powell's formula (1.1), but rather to underscore the need for its careful application. Although the convection velocity of large-scale coherent structures

is important, discussions on the disturbance convection velocity are limited due to the challenging nature of such measurements. This is because the introduction of a sensor in the jet shear layer can alter the feedback loop and modify the entire flowfield, which renders such intrusive disturbance convection velocity measurements meaningless.

Hence, the need arises for non-intrusive measurement techniques, such as particle image velocimetry measurements (Krothapalli et al. 1999), high-speed schlieren visualisation (Knast et al. 2018) and computational fluid dynamics simulations (Bogey & Gojon 2017). Additionally, the complexity and size of these datasets present challenges in their processing to extract reliable convection velocities. The scarcity of available velocity data limits discussions on the impact of disturbance convection velocity. Despite the challenges in reliably measuring the convection velocity, it is valuable to uncover its effect for an improved understanding of the physics of impinging jet flows. In the present study, schlieren flow visualisation with high-speed imagery is used to acquire a substantial amount of convection velocity data. Extracting convection velocity from schlieren visualisation can be achieved through modal decomposition methods such as DMD or SPOD. However, these methods entail additional computational costs. Another way is to construct wave diagrams, also known as space and time diagrams. While this method has been successfully employed in the past (Knast et al. 2018), its implementation necessitates the utilisation of highly time-resolved images that surpass the capabilities of typical laboratory-grade cameras. For instance, in the present study's data acquisition setup, images are captured at a frequency of 31 kHz, allowing for fewer than four images to be acquired during a single phase of impingement resonance (at 8 kHz) (Song et al. 2022a). Despite the 31 kHz sampling rate, simply arranging the acquired images in consecutive order is insufficient to reliably extract the convection velocity due to the limited number of images per phase, resulting in noisy wave diagrams. Hence, the present study employs a phase-bin-averaging method where schlieren images are rearranged and binned based on the phase of the impingement tonal frequency, which is obtained from acoustic measurements. This is particularly effective because impinging jets typically resonate at a single intense discrete tone. The details of this approach are discussed in § 2.2. Using this method, reliable convective velocity data are obtained over a wide range of conditions.

In the present study, the flowfields of a Mach 1.5 supersonic nozzle are examined across various NPRs and impingement distances. It is worth noting that the convection velocity measurement cases in this study primarily focus on the axisymmetric dominant mode. This choice is made because the frequency of impingement tones associated with the non-axisymmetric mode exhibits a weaker dependence on the impingement distance (Song *et al.* 2021).

The impingement frequencies do not vary significantly even when NPR is varied over a wide range. To explore the relationship among the variables in (1.1), acoustic measurements are performed under various NPR conditions to identify a range of NPR values where the impingement frequency remains relatively constant. Subsequently, time-resolved schlieren images are obtained to measure the convection velocity within this range of constant-frequency NPR values. A parametric study is then conducted to assess the relationship among the pertinent variables.

Variations in convection velocity across a range of impingement distances are investigated for both over- and ideally expanded jet conditions. The effect of convection velocity on the noise level and size of coherent structures is analysed. Additionally, the influence of the time interval between the reflected acoustic wave and the large-scale coherent structure on the boundary of the wall jet is examined. An acoustic speed-based frequency formula is proposed, and the vortex-sheet model (Tam & Ahuja 1990) is

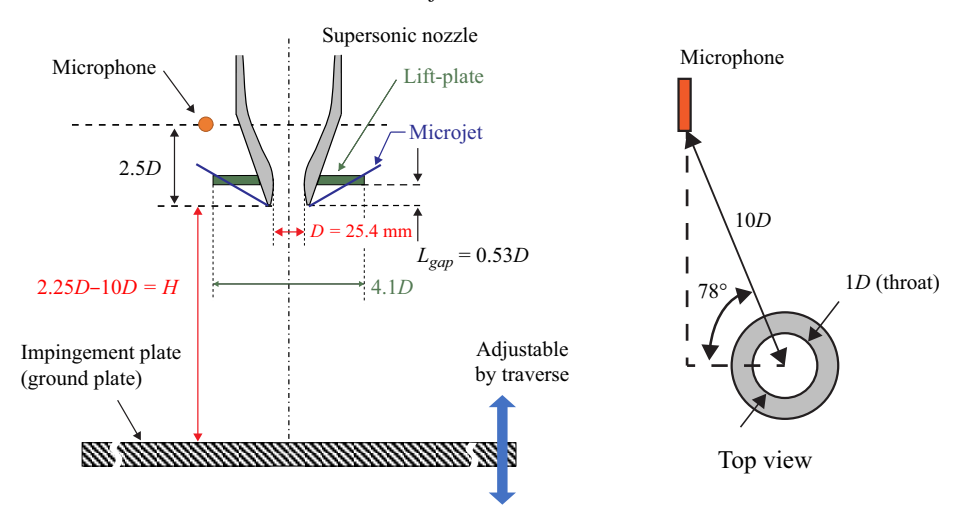


Figure 2. Schematics of experimental set-up and location of microphone (not to scale).

employed to determine the allowable frequency range of impingement tones. The acoustic speed-based model is validated using experimental data under various jet expanding NPR conditions, both with and without a lift plate, thereby providing a measure of confidence in the proposed approach.

2. Experimental set-up

2.1. Nozzle and measurement techniques

Experiments were performed at the Florida Center for Advanced Aero-propulsion located at Florida State University. A schematic diagram of the experimental set-up is shown in figure 2. A circular Mach 1.5 nozzle with a throat diameter (D) of 25.4 mm is used. A flow straightener is installed upstream of the nozzle. Compressed air, from high-pressure tanks (114 m³, 3440 kPa), is supplied to the system. The pressure in the stagnation chamber is controlled by a control valve and to maintain target pressure within an uncertainty of ± 0.02 NPR. A ground plate is positioned perpendicular to the jet axis. During nozzle operation, the temperature in the stagnation chamber is maintained at 288 ± 5 K, which also serves as the jet stagnation temperature. The temperature within the facility is 293 ± 3 K.

Sixteen microjet actuators with an exit diameter of 400 μ m are positioned at the lip of the nozzle. A lift plate, which can be detached as needed, holds the microjets and acts as a large reflective surface for acoustic waves. The lift plate has a diameter of 4.1D and its lower surface is situated at a distance of $0.53D_{-0.05D}^{+0}$ from the nozzle's exit plane (i.e. $L_{gap} = 0.53D$). The lift plate is intentionally left uncovered without any acoustically absorbent material to simulate the fuselage in STOVL applications.

The present study considers three distinct boundary conditions near the nozzle. The 'clean-nozzle' case refers to a configuration in which the microjet device (i.e. the lift plate in figure 2) is not mounted, resulting in the absence of strong acoustic reflections from the nozzle's external boundary. The 'baseline' case represents the condition when the microjet device is installed but none of the microjets are activated. The 'microjet' case describes a condition in which all microjets are activated, but their total pressure is insufficient to suppress large-scale coherent structures, allowing these structures to remain discernible in schlieren images and wave diagrams. At higher microjet supply pressures, large-scale coherent structures tend to be substantially attenuated. However, this effect

is of limited relevance to the present study, as the absence of these structures precludes reliable and meaningful estimation of convection velocity. In this context, microjet control is employed primarily to modify disturbance convection velocity, rather than to significantly suppress large-scale coherent structures. For this reason, the present study focuses exclusively on cases with ineffective microjet control, selected from our large dataset encompassing various microjet configurations, to isolate and analyse the impact of disturbance convection velocity. Cases involving effective control, which significantly attenuate large-scale coherent structures, are excluded from this analysis and are not presented here. The effective attenuation of large-scale coherent structures using microjet control, along with the associated noise reduction informed by a genetic algorithm, is detailed in the studies by Song *et al.* (2023) and Song (2024).

Schlieren flow visualisation is carried out using a high-speed camera (Fastcam SA5 Photron, 12 bit). The set-up uses a Z-type arrangement with two identical parabolic mirrors (diameter, 304.8 mm; focal length, 2.54 m). For each case, a total of 8192 images are captured at a rate of 31 kHz. A white light (Luminus Device 7000 K light-emitting diode) is pulsed for a duration of 1 µs. Concurrently with the high-speed schlieren visualisation, microphone signal data are acquired for a duration of 5 s at a rate of 102.4 kHz. The schlieren set-up is affected by vibrations induced by the flow, which can result in image drift and global brightness variations. The drift in each image is corrected using cross-correlation computations. The location of the maximum cross-correlation value is determined at subpixel level using two-dimensional Gaussian regression (Nobach & Honkanen 2005), based on the cropped image near the supersonic nozzle exit in the first frame. Further details of the process of global brightness adjustment are documented by Song *et al.* (2022*b*).

A Brüel & Kjær Type 4939 microphone is used to acquire acoustic signals. The microphone is positioned 2.5D behind the nozzle exit plane and 10D away from the nozzle axis, as seen in figure 2. The microphone was calibrated using a pistonphone (Brüel & Kjær Type 4220). The microphone signal is acquired at a rate of 102.4 kHz using a deltasigma ADC (NI PCI-4472, 24bit) after being amplified through a Brüel & Kjær Type 2670 pre-amplifier and a Type 2692 NEXUS amplifier. To construct acoustic spectrograms (acoustic spectra versus impingement distance), acoustic measurements are performed at a step resolution of 0.0625D (1.6 mm). The ground plate is moved towards the nozzle from H/D of 10–2.25 using a traverse device equipped with a stepper motor. Acoustic data are acquired for 1 s at each impingement distance. Acoustic spectra are calculated using the Pwelch function in MATLAB. For acoustic spectrograms, a subset length of 2048, equivalent to a frequency resolution of 50 Hz, is used with a Hanning window and 75 % overlap. The frequency is normalised using the Strouhal number ($St = fD_i/U_i$). The fully expanded jet velocity (U_i) is equivalent to the ideally expanded jet velocity at a given NPR. The fully expanded jet diameter (D_i) , calculated by equation (13) in the work by Tam (1995), is equivalent to the exit diameter maintaining the same mass flow rate.

2.2. Convecting disturbances: identification and measurement using phase-conditioned image analysis

To determine the convection velocity of large-scale coherent structures, space–time (x-t) wave diagrams are constructed from schlieren image sets. The phase-bin-averaging method, depicted schematically in figure 3, is used in constructing these diagrams. An example case from the clean-nozzle condition at H/D = 4.19 and NPR = 3.0 is provided to illustrate the process. Images are captured at a frame rate of 31 kHz. However, this rate is

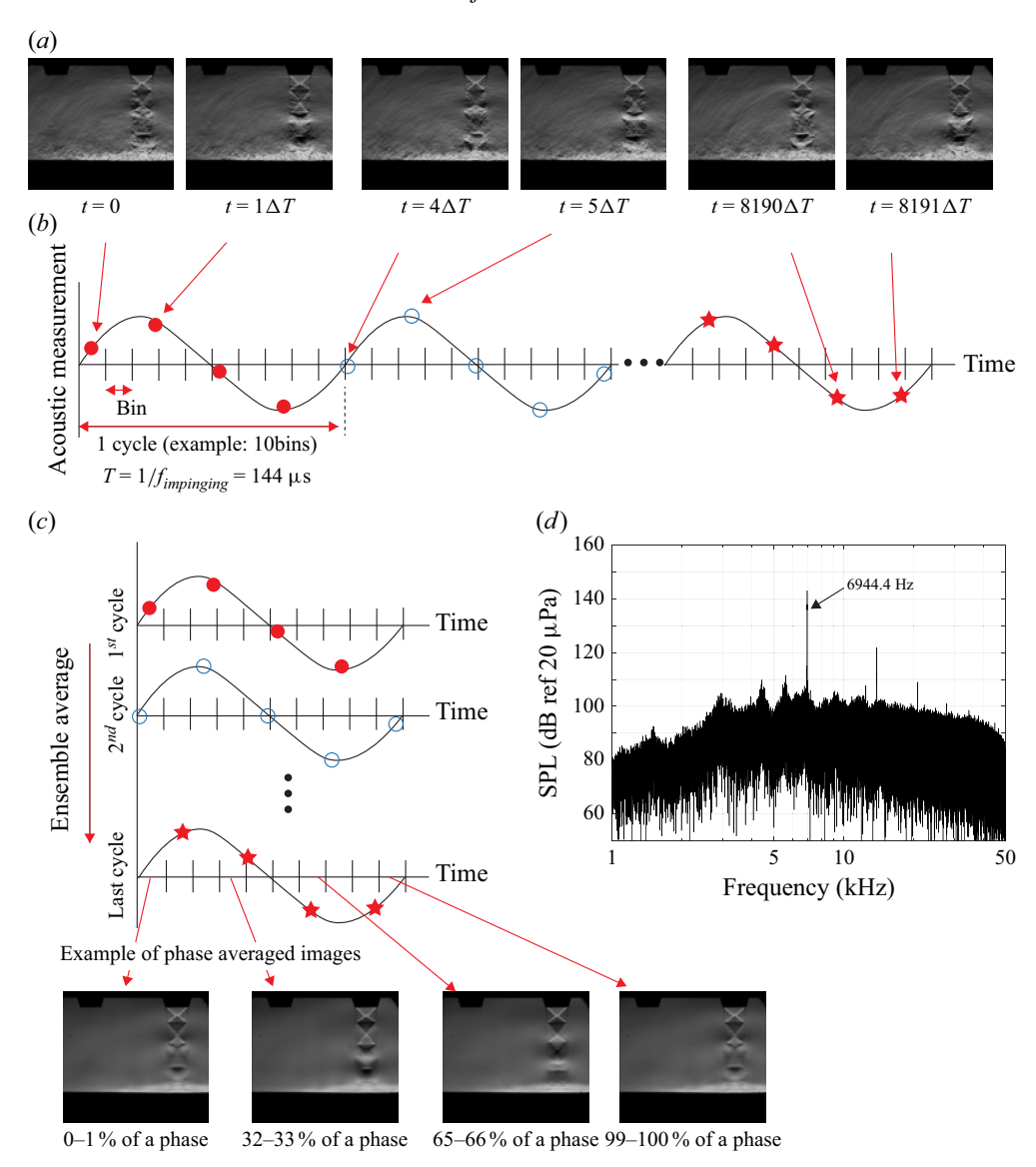


Figure 3. Schematic depiction of phase-bin-averaging method (H/D = 4.19 and NPR = 3.0). (a) Instantaneous schlieren images in a time series, (b) Phase binning based on acoustic measurements and image assignment, (c) Ensemble averaging of images and example phase-averaged images and (d) Acoustic spectrum.

insufficient to clearly resolve a specific coherent structure when the jet resonates at 7 kHz, as it permits the acquisition of fewer than six images during the convection time of a single coherent structure. To address the issue of insufficient frame rate, an approach is used that takes advantage of the repetitive nature of the flow caused by jet resonance at a known frequency for a given impingement tone. Each image can be assigned a phase based on its time stamp, aided by synchronised acoustic measurements. The reference phase period is obtained through acoustic measurements, revealing an impingement tonal frequency measurement of 6944.4 Hz (figure 3d). To achieve higher frequency resolution, a fast Fourier transform length of 51 200 at a sampling rate of 102.4 kHz is employed without using a subset, resulting in a frequency resolution of 0.2 Hz in the frequency domain.

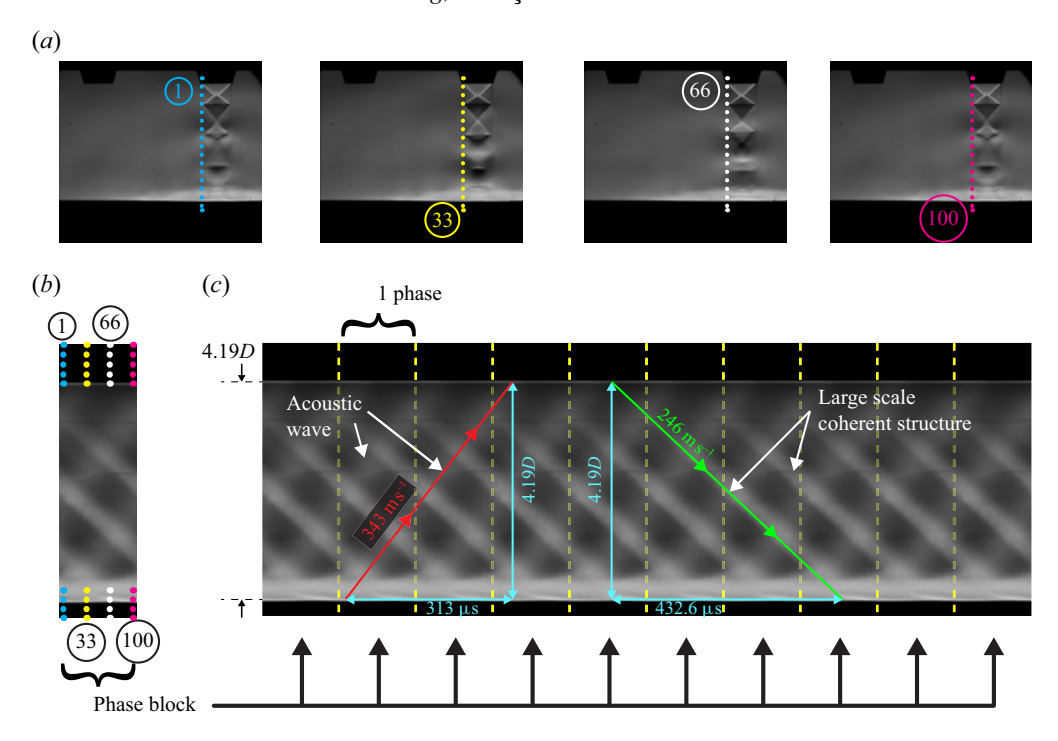
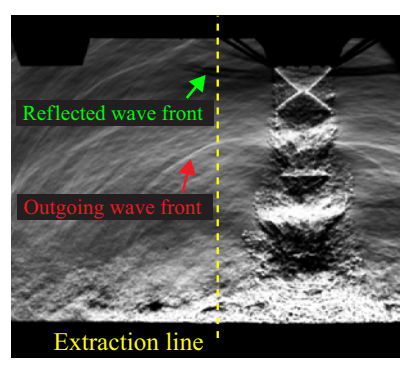


Figure 4. Construction of wave diagram from phase-bin-averaged images. (a) Phase-averaged images, (b) Phase block and (c) Wave diagram.

The timeline is divided into individual cycles based on the impingement tone, and each cycle is further discretised into 100 bins. For brevity's sake, only 10 bins are shown as an example in figure 3. Each image is then assigned to its corresponding time bin based on its capture time (figure 3b). By taking the ensemble average of the images within the same bin across multiple cycles, a phase-averaged image is obtained for each bin (figure 3c). Examples of phase-averaged images for the 1st, 33rd, 66th and 100th bins are provided in the bottom row of figure 3.

To determine the convection velocity of large-scale coherent structures, a time-image intensity plot (i.e. wave diagram) is generated using the phase-bin-averaged images. The process of constructing the wave diagram is described in figure 4. From the phase-averaged images, as depicted at the bottom of figure 3, intensity profiles along the dotted line are extracted from each phase-bin-averaged image (a total of 100 bins), as shown in figure 4(a). Four different phase images (1st, 33rd, 66th, 100th) are provided as an illustrative example. These extracted intensity profiles are then arranged in consecutive phase bins along the x axis, forming a phase block (figure 4b). By sequentially arranging the phase blocks, a wave diagram is constructed (figure 4c). In the example wave diagram, 10 identical phase blocks are used. The yellow dashed lines in the wave diagram represent the borders between two adjacent phase blocks. Notably, discernible traces from each phase block are smoothly connected across the adjoining phase blocks. Two noticeable diagonal traces can be observed appearing as brighter lines. The upward trace in red represents the trajectory of acoustic waves, while the downward trace in green corresponds to the large-scale coherent structures. The horizontal axis in the diagram represents phase (or time), while the vertical axis represents the distance coordinate. The speed of the trace can be determined by its slope $(\Delta x/\Delta t)$. For instance, the green downward line in figure 4 represents the



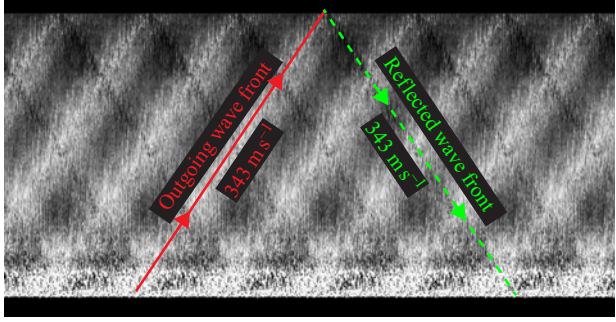


Figure 5. An example wave diagram with the first image of each bin (data from outside the jet column).

average disturbance convection velocity ($C_{st,mean}$) of 246 m s⁻¹. The line representing the disturbance convection velocity is drawn parallel to the downward trace once the coherent structure has sufficiently developed as it convects downward. The convection velocity error is estimated to be within ± 10 m s⁻¹. In figure 4, a red upward line is drawn with a slope of 343 m s⁻¹, which corresponds to the speed of sound at 20 °C. This line exhibits a close alignment with the upward trace, which represents the propagation of acoustic waves upstream.

Once the impinging jet experiences an intermittent tone shift and then reverts, the trace of the large-scale coherent structure in the phase-averaged wave diagram may become blurred. Under this condition, a different type of wave diagram is employed, and an example result is presented in figure 5. In this case, the extraction line is positioned outside the jet shear layer, resulting in the absence of convection velocity information in the wave diagram. It is worth noting that the extraction line outside the jet shear layer in figure 5 serves only as an illustrative example, and the convection velocity reported in this study is measured based on the extraction line along the nozzle exit edge, as shown in figure 4. Unlike the method that uses phase averaging, as explained in figure 3, the wave diagram in figure 5 is constructed using a single image from each bin (i.e. ensemble averaging is omitted). This approach results in a noisier but sharper representation, enhancing the visibility of the reflected wavefront traces, which appear as dark lines (highlighted with a green dashed line). This reflected wavefront is not discernible in the phase-averaged wave diagram, as it becomes smeared out due to its slightly inconsistent location in the images within each phase bin.

Since SPOD can extract modes at the impingement tonal frequency, it enables reconstruction of a wave diagram similar to that shown in figure 4, by replacing the phase-averaged images with the temporal evolution of SPOD modes. Accordingly, a wave diagram based on SPOD is constructed and compared with one obtained from phase-bin-averaged images, both derived from the same schlieren image set at H/D = 4.19, NPR = 3.67, for the baseline case (i.e. with the lift plate present). The comparison is presented in figure 6. The SPOD analysis is performed in MATLAB using the code provided by Towne *et al.* (2018). Figures 6(a) and 6(c) show the phase-bin-averaged image and the dominant SPOD mode shape, respectively. Supplementary movies 1 and 2, available at https://doi.org/10.1017/jfm.2025.10688, illustrate the full phase evolution. The yellow dashed extraction lines shown in figures 6(a) and 6(c) are located at the same position. The resulting wave diagrams constructed along these extraction lines are shown in figures 6(b) and 6(d), respectively. The upper section of the wave diagrams, corresponding to the vicinity of the nozzle, is omitted, as the initial disturbance does

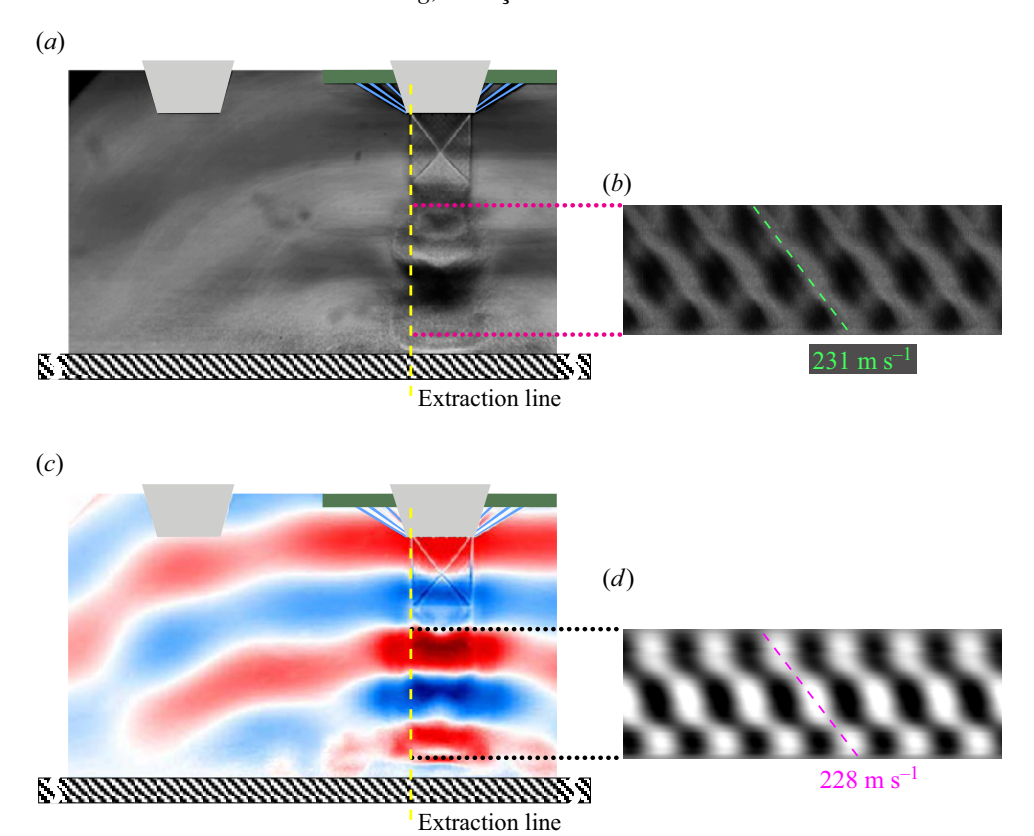


Figure 6. Comparison of wave diagrams constructed from phase-averaged images and first SPOD mode at impingement frequency for the baseline case at H/D = 4.19 and NPR = 3.67. (a) Phase-averaged schlieren image, (b) Wave diagram from phase-averaging, (c) First SPOD mode shape and (d) Wave diagram from first SPOD mode (converted to greyscale for comparison).

not grow significantly or become dominant compared with the upstream-propagating acoustic waves. It is worth noting that acoustic waves are captured by both methods, since the collimated light used in schlieren imaging passes through the entire field of view, as seen in figure 6(a). The bottom region of the image is also excluded from this analysis, as light rays propagate through the wall jet – a region outside the scope of the disturbance convection. As discussed, the disturbance convection velocities in this paper are evaluated using the regions of the wave diagrams. In figure 6, this region is indicated by dotted lines as a representative example. However, except in figure 6, the convection velocity lines have been extrapolated up to the nozzle and the ground plate for clarity and readability. For clearer comparison, the SPOD wave diagram in figure 6(d) has been converted to greyscale. The wave diagram based on phase-bin averaging (figure 6b) reveals a reasonably smooth and connected downstream convection of coherent structures. The green downward dashed line represents a disturbance convection velocity of 231 m s⁻¹. The SPOD-based wave diagram (figure 6d) exhibits similar behaviour but with a more staircase-like structure, displaying a somewhat saw-toothed pattern. As in the phaseaveraged method, the magenta dashed line indicates the convection velocity. It provides a very similar estimate of the convection velocity, 228 m s⁻¹, to that obtained from the phase-averaged wave diagram, confirming the parallel between the two approaches, as

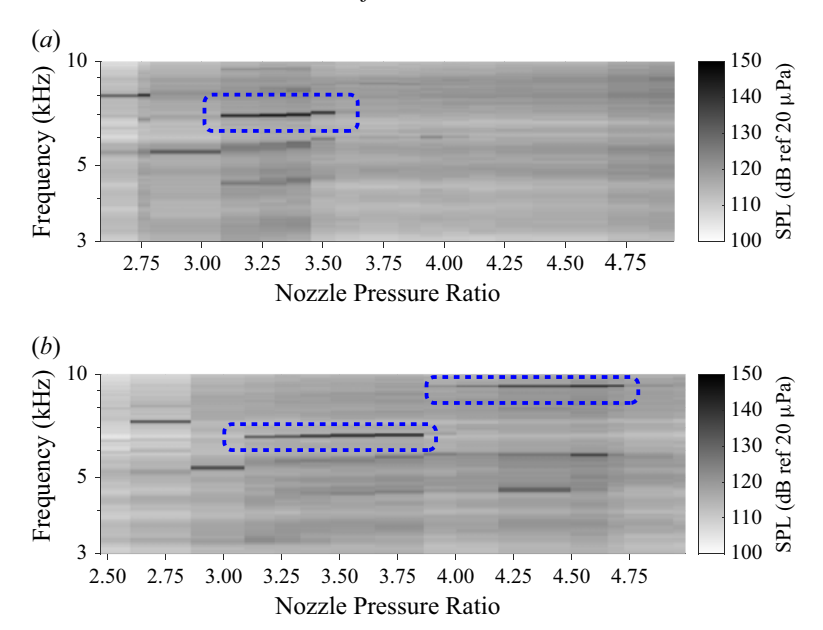


Figure 7. Impingement tonal frequency variation across a range of NPRs for clean-nozzle case at (a) H/D = 4.19 and (b) H/D = 5.44. Blue dashed box highlights nearly constant frequency of impingement tone.

expected. Nevertheless, the phase-averaged method is used to construct the wave diagrams for determining the convection velocity, due to its clearer interpretability.

3. Effect of NPR on impingement tone frequency

According to (1.1), the disturbance convection velocity is an important variable in determining impingement tonal frequency. Nevertheless, even though different NPRs lead to changes in convection velocity (Krothapalli *et al.* 1999), the impingement tonal frequency itself does not vary significantly across various NPRs (Powell 1988). To better understand this apparent contradiction, the impingement tones are measured over a wide range of NPRs. A subset of these data is used to identify the range of NPRs that result in a consistent, i.e. nearly fixed, impingement frequency. Using this subset NPR, it becomes possible to assess the relationships among the variables in (1.1) while disregarding abrupt shifts in impingement frequency caused by staging.

The impingement tonal frequency behaviour under varying NPR conditions for cleannozzle cases at H/D of 4.19 and 5.44 is presented in figure 7. The conversion of frequency to Strouhal number is not applied since the scaling of the Strouhal number depends on NPR (i.e. a change in NPR results in variations in both M_j and D_j). Darker lines correspond to high-intensity discrete sound pressure level (SPL), indicative of impingement tones. As NPR increases, a slight elevation in tonal frequency can be seen as highlighted by dashed boxes, accompanied by sudden changes in frequency due to staging. Similarly, figure 8 shows the impingement tonal behaviour for the baseline case with the lift plate installed, at H/D of 4.19 and 5.44. Impingement tonal frequencies, highlighted by the dashed lined boxes, remain consistent for the NPR range of 3–4.3, as seen in figure 8. The spectrograms of the baseline cases, as shown in figure 8, demonstrate a wider range of NPR for maintaining a nearly constant impingement tonal frequency compared with

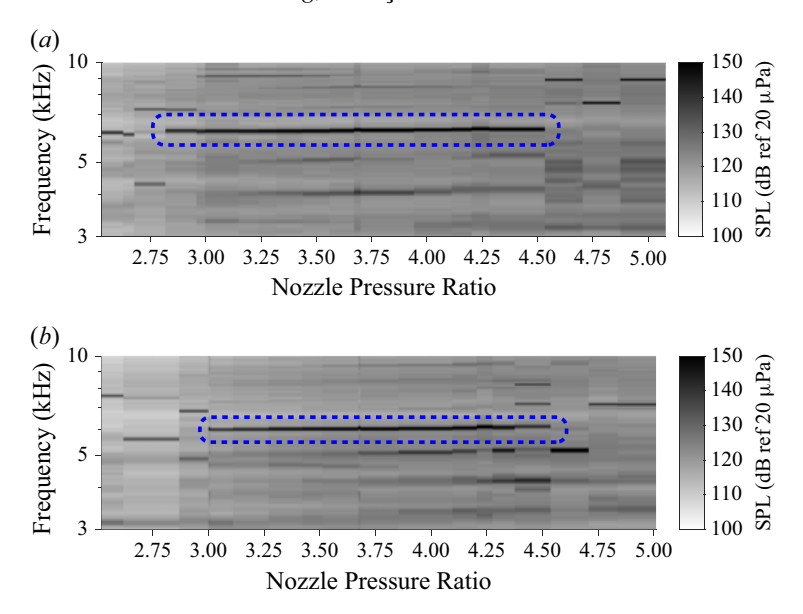


Figure 8. Impingement tonal frequency variation across a range of NPRs for baseline case at (a) H/D = 4.19 and (b) H/D = 5.44. Blue dashed box highlights nearly constant frequency of impingement tone.

the clean-nozzle cases presented in figure 7. This observation suggests that the presence of a reflective surface, such as the lower surface of the lift plate, extends the NPR range where the impingement tonal frequency remains nearly constant. It is noteworthy that this phenomenon of a nearly constant frequency differs from the screech tonal frequency (associated with a free jet) (Krothapalli *et al.* 1999), which is more influenced by variations in NPR. Although changes in NPR induce only minor frequency variations within the blue dashed boxes in figures 7 and 8, there is a discernible trend of frequency slightly increasing with a rise in NPR. This suggests that within the nominal 'fixed frequency' range, small changes in the impingement tonal frequency may be attributed to corresponding changes in disturbance convection velocity caused by varying NPR, in accordance with (1.1).

To explore this, the relationships among the variables in (1.1) are evaluated, specifically focusing on the impingement tones that maintain a nearly constant frequency within the dashed-line boxes depicted in figure 8. The baseline cases are selected over the cleannozzle cases for the relationship evaluation due to their broader NPR range, which supports a nearly constant frequency; additionally, this broader NPR range is expected to produce a perceptible difference in the disturbance convection velocity. Time-resolved schlieren image sets are acquired for NPR conditions of 3, 3.67 and 4.2 at H/D = 4.19 and 5.44. These NPR conditions are chosen based on the range in figure 8 where the impingement frequency remains nearly constant. Wave diagrams are constructed for NPRs of 3, 3.67 and 4.2 to determine the mean convection velocities of shear-layer instability, C_{st.mean}. The resulting wave diagrams are presented in figure 9, where the left-hand column corresponds to H/D = 4.19 and the right-hand column to H/D = 5.44. The chart is structured in three rows, each representing a different condition: the top row for overexpansion (NPR = 3), the middle row for ideal expansion (NPR = 3.67) and the bottom row for underexpansion (NPR = 4.2). The lines used to extract the convection velocities are colour-coded: a green solid line for NPR = 3, a magenta dashed line for NPR = 3.67 and a yellow dotted line for NPR = 4.2. The ideally expanded condition (NPR = 3.67) will henceforth be referred

to as a reference condition for comparison in subsequent discussions. For ease of slope comparison, magenta dashed lines representing the convection velocity at NPR = 3.67 are overlaid with a single phase distance (T_{period}) in other NPR conditions. For both impingement distances, it is observed that the slope becomes steeper with increasing NPR. This suggests that a higher NPR leads to an increase in the disturbance convection velocity.

The convection velocities derived from the wave diagrams in figure 9 and the corresponding impingement frequencies are organised in table 1. Although an increase in NPR results in a rise in both the convection velocity ($C_{st,mean}$) and frequency of impingement tone, the variation in the impingement tonal frequency from the reference condition is negligible, remaining within 1 %. Notably, the relative deviation in frequency is significantly smaller than that of the convection velocity, suggesting concomitant changes in the phase (P) in (1.1). To further investigate the impact of these variables on impingement frequency, a parametric analysis is performed using (3.1):

$$\frac{N_{stage} + P}{f_{impinging}} = \frac{H + 2L_{gap}}{C_a} + \frac{H}{C_{st,mean}}.$$
 (3.1)

Equation (3.1) is a simplified version of (1.1), wherein the integral term is substituted by the mean convection velocity ($C_{st,mean}$). The upstream acoustic wave travel time term now includes the gap distance (L_{gap}) . This inclusion accounts for the influence of a wide reflective surface, positioned behind the nozzle exit, on the impingement tonal frequency (Song et al. 2022a). In a clean-nozzle configuration, with the lift plate absent, L_{gap} is considered to be zero. Conversely, when the lift plate is present – as in the baseline and microjet cases – L_{gap} is set to 0.53D. Initially, the integer N_{stage} is established using (3.1) for the reference condition, which is the ideally expanded condition. It is worth noting that the value of N_{stage} remains unchanged across all three NPR conditions due to the absence of any sudden changes in frequency, meaning no staging occurs. The geometric dimensions determine the H and L_{gap} values, and the acoustic wave speed (C_a) is 343 m s⁻¹ at a room temperature of $20\,^{\circ}$ C. Upon substituting the measured $f_{impinging}$ and $C_{st,mean}$ values of the reference condition, the unknown variables are N_{stage} and P in (3.1). Given the phase range of -1 < P < 1, the integer N_{stage} is selected such that the phase value is nearest to zero. This leads to a corresponding phase value ($P_{@reference}$), which is approximately 0.31 for both impingement distance conditions. The corresponding integer values (N_{stage}) are 5 for H/D = 4.19 and 6 for H/D = 5.44. It is worth noting that staging occurs once between H/D = 4.19 and 5.44, near H/D of 4.25 (Song et al. 2022a), which aligns with the relationship $N_{stage@H/D=4.19}+1=N_{stage@H/D=5.44}$. Further insights into the integer N_{stage} and phase lead/lag (P) are provided in the context of a wave diagram example in § 6.1.

The effect of convection velocity variation on the impingement tonal frequency at H/D=4.19 and 5.44 is summarised in figure 10. The dashed line, calculated using (3.2), represents the frequency change due to the convection velocity variation, assuming a constant phase of $P=P_{@reference}\approx 0.31$. Equation (3.2) is a rearranged version of (3.1) with regard to the impingement tonal frequency. The circular symbols denote the measured frequencies, and the dashed line of calculated frequencies intersects with the reference point, as these calculations are based on the reference point. Although the difference between the calculated and measured frequencies is relatively small, the variation in frequency – not the frequency itself – due to changes in convection velocity is overpredicted when the phase value is held constant. This observation supports that the phase value varies as the disturbance convection velocity changes.

M. Song, S. Seçkin and F.S. Alvi

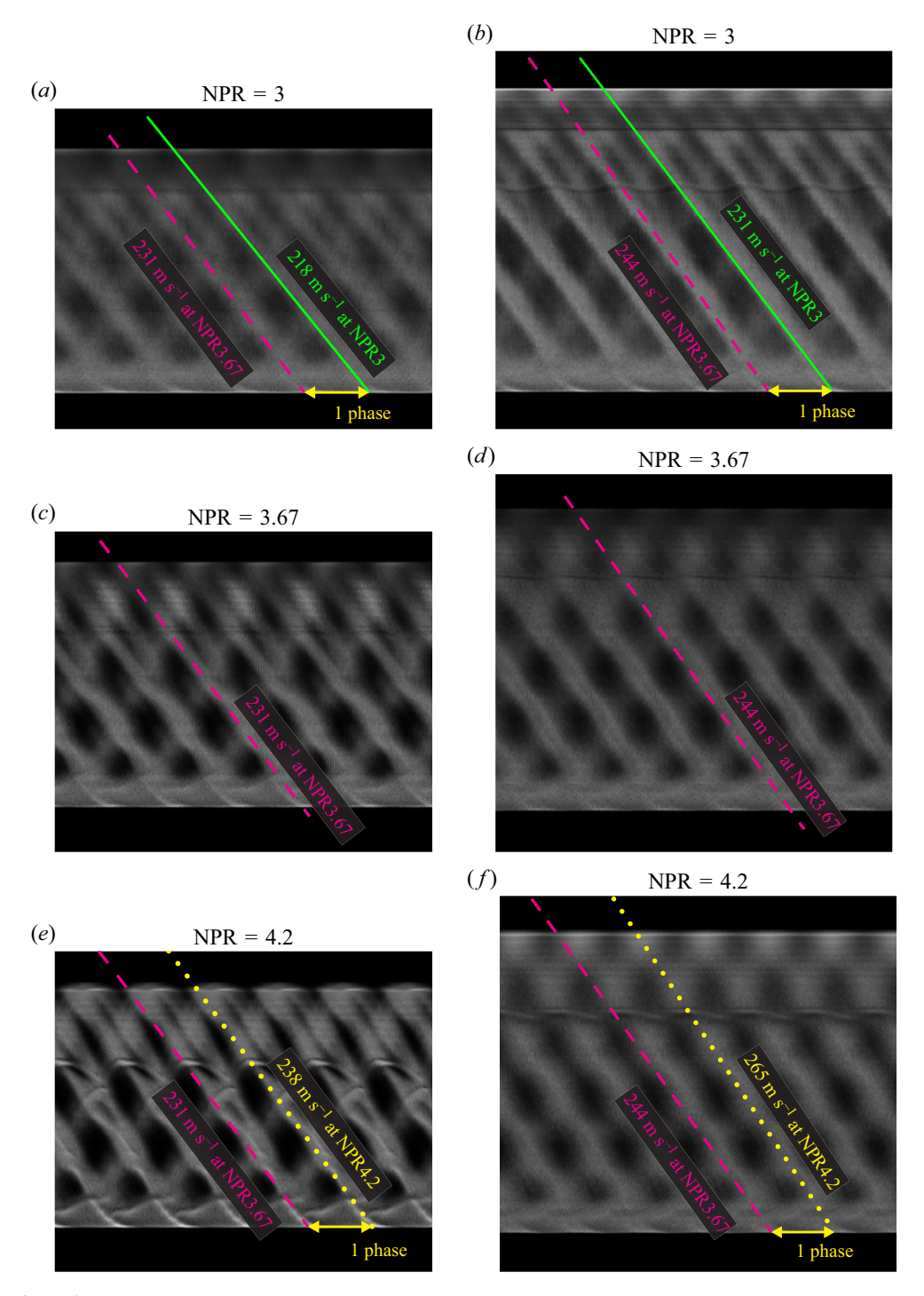


Figure 9. Wave diagrams to obtain disturbance convection velocity ($C_{st,mean}$), represented by the slope of the line: (a,c,e) H/D = 4.19; (b,d,f) H/D = 5.44. The dashed lines in magenta indicate the convection velocity at NPR of 3.67 for each H/D and are provided as a reference.

	Fully expanded	H/D = 4.19		H/D = 5.44	
NPR	jet velocity, U_j (m s ⁻¹)	$C_{st,mean} \text{ (m s}^{-1})$	$f_{impinging}$ (kHz)	$C_{st,mean} \text{ (m s}^{-1})$	$f_{impinging}$ (kHz)
3 (over)	395 (-6.8 %)	218 (-5.6 %)	6.20 (-0.8 %)	232 (-4.9 %)	5.99 (-0.7 %)
3.67 (ideal)	424	231	6.25	244	6.03
4.2 (under)	441 (+4.0 %)	238 (+3.0%)	6.29 (+0.6%)	265 (+8.6%)	6.08 (+0.8%)

Table 1. Convection velocity of coherent structure and impingement tonal frequency for different NPRs. The values in parentheses are deviations based on the ideally expanded case (NPR = 3.67).

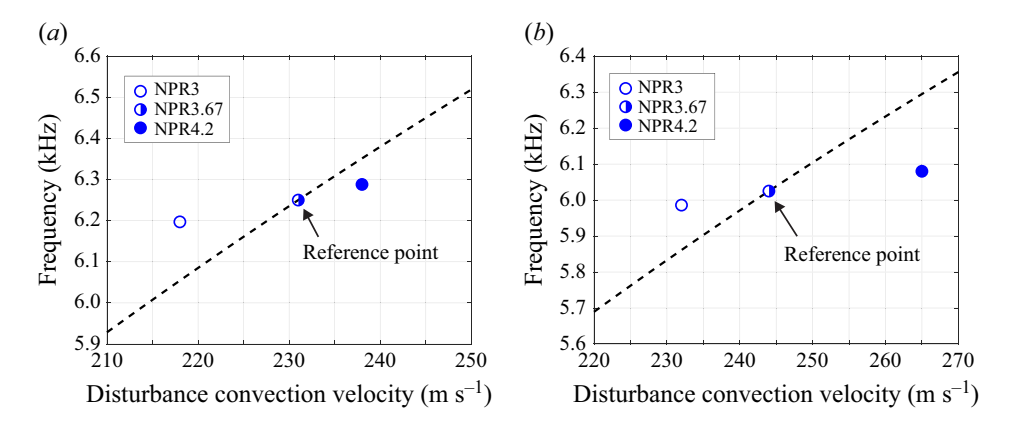


Figure 10. Effect of convection velocity on impingement frequency (nearly constant) at (a) H/D = 4.19 and (b) H/D = 5.44. Dashed lines, calculated by (3.2), represent frequency variation while phase value is fixed to be the corresponding $P_{@reference}$. Corresponding conditions are presented in table 1.

$$f_{impinging} = \frac{N_{stage} + P_{@reference}}{\frac{H + 2L_{gap}}{C_a} + \frac{H}{C_{st\ mean}}}.$$
(3.2)

This raises the question of how the phase (P) varies to keep the impingement frequency nearly constant, as experimentally measured. To resolve this, another parametric analysis is performed in a fashion similar to that before by reorganising (3.1) into (3.3):

$$P = f_{@reference} \left(\frac{H + 2L_{gap}}{C_a} + \frac{H}{C_{st,mean}} \right) - N_{stage}.$$
 (3.3)

By holding the impingement tonal frequency constant at the reference condition value, the phase lead/lag is calculated using (3.3) and depicted as a dashed line in figure 11. The circle symbols represent the measured phase by substituting the measured frequency into $f_{@reference}$ in (3.3). The error bars indicate the range of phase values obtained by propagating the estimated convection velocity error ($\pm 10 \,\mathrm{m\,s^{-1}}$) through the phase value calculation. The trend of measured phase agrees with that of the calculated phase (i.e. dashed line) across different convection velocities, as seen in figure 11. The change in phase across NPR is not negligible compared with the available range of phase value (-1 < P < 1). It is noteworthy that in figure 11 the phase values for the two impingement distances (H/D = 4.19 and 5.44) are similar for both over- and ideally expanded conditions. However, these phase values are not necessarily consistent across impingement distances. For example, in the underexpanded condition (NPR = 4.2), there

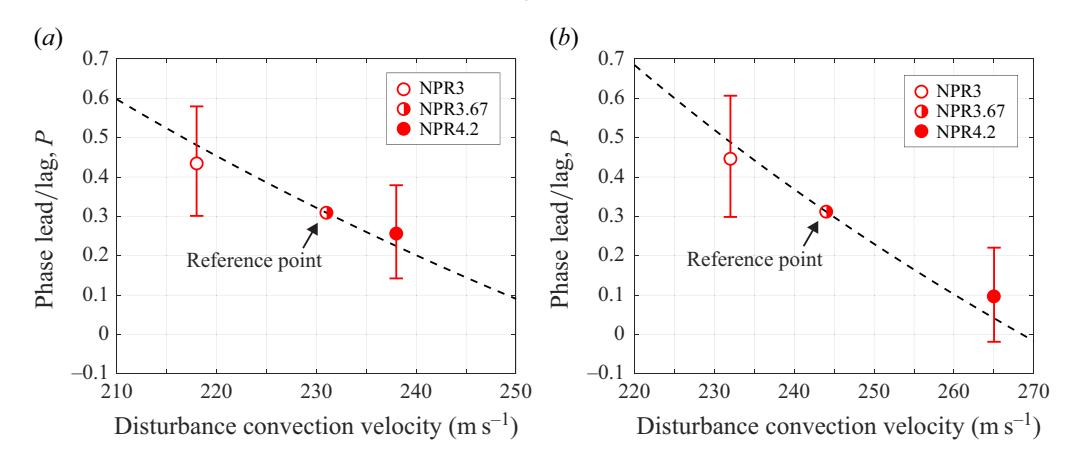


Figure 11. Effect of convection velocity on phase lead/lag at (a) H/D = 4.19 and (b) H/D = 5.44. Dashed lines, calculated by (3.3), represent phase variation while tonal frequency is fixed to be the corresponding $f_{@reference}$. The corresponding conditions are presented in table 1.

is a noticeable difference in phase values in figures 11(a) and 11(b). After all, the observations underline that the convection velocity and phase are expected to vary under different NPR conditions when using (1.1), as it describes the mechanism of jet resonance.

4. Effect of impingement distance on convection velocity and relation among convection velocity and resonance properties

The variation in convection velocity for the overexpanded jet (NPR = 3) across various impingement distances is obtained from wave diagrams. These results are shown in figure 12(a), where the baseline case is represented by blue circles and the microjet case is depicted by red squares. An estimated error bar for the convection velocities is provided on one of the data points. The corresponding acoustic spectrogram for the baseline case is presented in figure 12(b); the tonal frequencies of the baseline and microjet control cases are denoted by blue circles and red squares, respectively, on top of the baseline acoustic spectrogram. The microjet cases are included here to reveal their influence, if any, on the disturbance convection velocity. However, it should be noted that the selected microjet control cases in the present study do not entirely eliminate largescale coherent structures. Consequently, large-scale coherent structures remain sufficiently distinguishable to obtain their convection velocity, as exemplified by the instantaneous schlieren images in figure 12(c). In general, the activation of microjets results in an increase in the convection velocity as it attenuates the axisymmetric coherent structures in the jet shear layer. Those interested in shear-layer properties are referred to studies on the effects of microjets (Arakeri et al. 2003; Alvi et al. 2008), instability modelling (Schmidt et al. 2017; Lesshafft et al. 2019) and the impact of the incoming boundary layer on jet noise (Bogey & Bailly 2010; Brès et al. 2018). The red square symbols overlap with the baseline impingement frequency as seen in the spectrogram, indicating that the elevated convection velocity due to microjet activation does not modify the impingement tonal frequency unless the control mechanism induces staging behaviour. For instance, when the microjet is activated near the end of a stage (e.g. H/D = 4.4 and 5.5), the impingement tonal frequency tends to shift to the next stage, accompanied by a step change of 0.1 in $C_{st.mean}/U_i$, which translates to an ~ 20 % increase in convection velocity. For the baseline

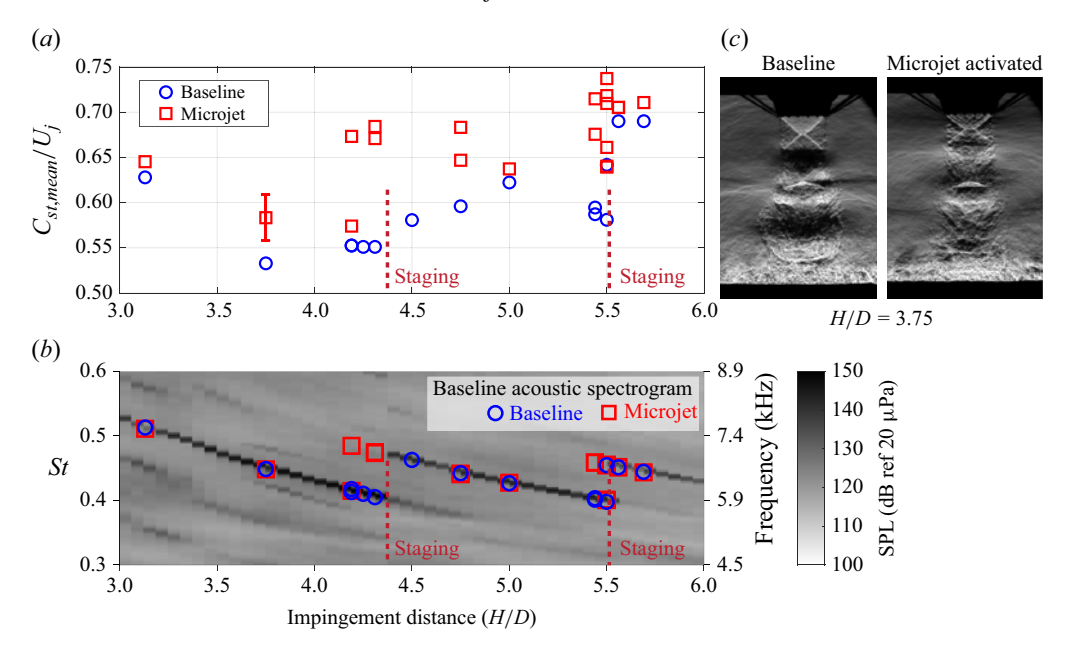


Figure 12. Variation of convection velocity and baseline acoustic spectrogram across various impingement distances (M = 1.5, NPR = 3, axisymmetric mode only). (a) Convection velocity distribution, (b) Corresponding tonal frequencies at convection velocity measurement points on top of the baseline acoustic spectrogram and (c) Instantaneous flowfield.

case, represented by blue circle symbols in figure 12(a), convection velocities exhibit a sudden surge near H/D = 5.5 during the stage transition, triggered by a minor increase in H/D. However, near H/D = 4.4, the rise in the baseline convection velocity across the staging is less pronounced than the velocity increase observed near H/D = 5.5. The observation indicates that frequency staging and a surge in convection velocity are not necessarily causally linked, despite the possibility of staging occurring alongside a change in convection velocity.

In a similar fashion, figure 13(a) shows the variation in convection velocity for the ideally expanded condition across various impingement distances. Microjet activation leads to an increase in the convection velocity. Specifically, near the end of a stage at H/D=6.2, the activation of microjets triggers a shift to the subsequent stage (i.e. the frequency jumps to that of the next stage), accompanied by an increase in the convection velocity. On the other hand, near H/D=4.6, microjet activation elevates the convection velocity, while the impingement tonal frequency remains unchanged. These findings are consistent with the trends observed in the overexpanded jet condition, as depicted in figure 12. These results suggest that the influence of convection velocity on impingement tonal frequency is marginal, except when staging behaviour is involved. For the baseline case, the convection velocity gradually increases as the impingement distance increases where H/D > 4, as shown in figure 13(a). However, in the overexpanded jet case depicted in figure 12(a), the convection velocity does not consistently increase. Consequently, it is challenging to identify a discernible trend in the convection velocity with respect to the impingement distance or frequency.

The disturbance convection velocities obtained in previous studies, which employed a nozzle with the same design Mach number and NPR range (Krothapalli *et al.* 1999; Bogey & Gojon 2017), are also included for comparison in figure 13. The diamond symbols

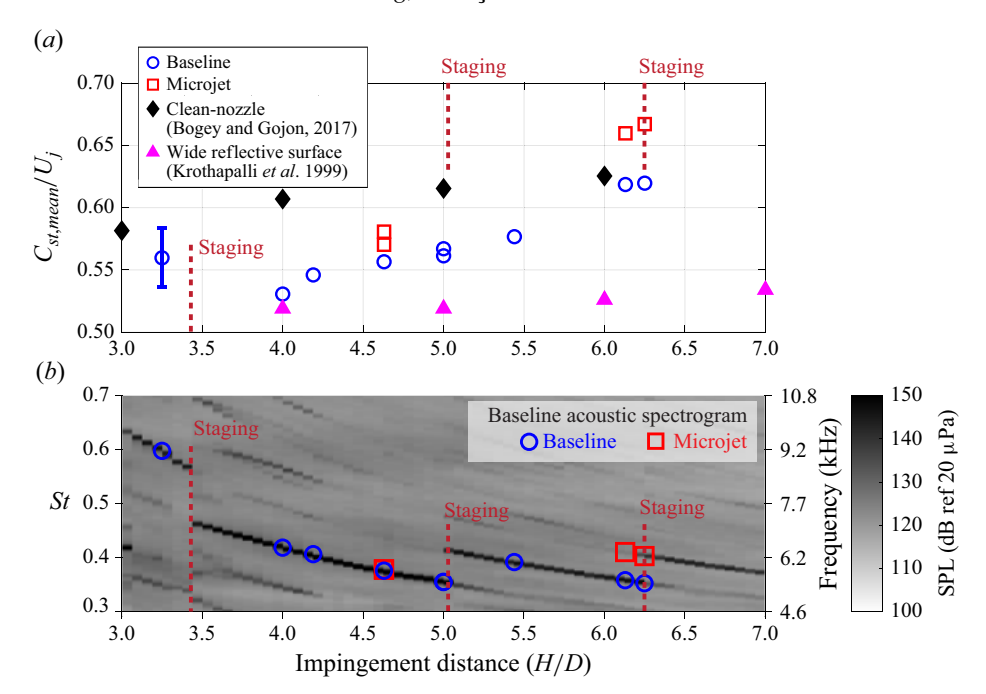


Figure 13. Variation of convection velocity and baseline acoustic spectrogram across various impingement distances (M = 1.5, NPR = 3.67, axisymmetric mode only). (a) Convection velocity distribution and (b) Corresponding tonal frequencies at convection velocity measurement points on top of the baseline acoustic spectrogram.

(Bogey & Gojon 2017) represent data obtained from a clean nozzle, while the triangle symbols (Krothapalli et al. 1999) correspond to a nozzle equipped with a circular lift plate of 10D in diameter. In contrast, the lift-plate diameter used in the present study is 4.1D. In general, all three sets of disturbance convection velocities exhibit a gradual rise with an increase in impingement distance. While there is a general agreement, there are, however, notable convection velocity differences in the present data from those earlier investigations. To examine how different acoustic reflective conditions influence the size of large-scale coherent structures, their convection velocity and the resultant noise, a comparison is made using instantaneous schlieren images as shown in figure 14. These images show the clean-nozzle and baseline cases under an overexpanded jet condition (NPR = 3) at an impingement distance of 4.19. The presence of an acoustic reflective surface (i.e. when the lift plate is mounted) leads to a larger size of large-scale coherent structures and a higher overall SPL (OASPL) compared with the clean-nozzle case (i.e. corresponds to the diamond symbols in figure 13). Here the baseline case exhibits a slower convection velocity ($C_{st,mean}/U_i = 0.55$) compared with the corresponding clean-nozzle case ($C_{st,mean}/U_i = 0.62$). This observation suggests that a larger reflective surface near the nozzle exit intensifies jet resonance, which in turn leads to a decrease in disturbance convection velocity (concomitant with larger coherent structures). This explains the difference in convection velocity under the same nominal conditions as in figure 13. In other words, the clean-nozzle case (represented by diamond symbols) exhibits a higher convection velocity along with weaker jet resonance and smaller coherent structures. As the reflective surface widens, the jet resonance strengthens, leading to lower convection velocities of larger coherent structures. The external geometry of the nozzle has a strong influence on the feedback loop - for example, resulting in a shift

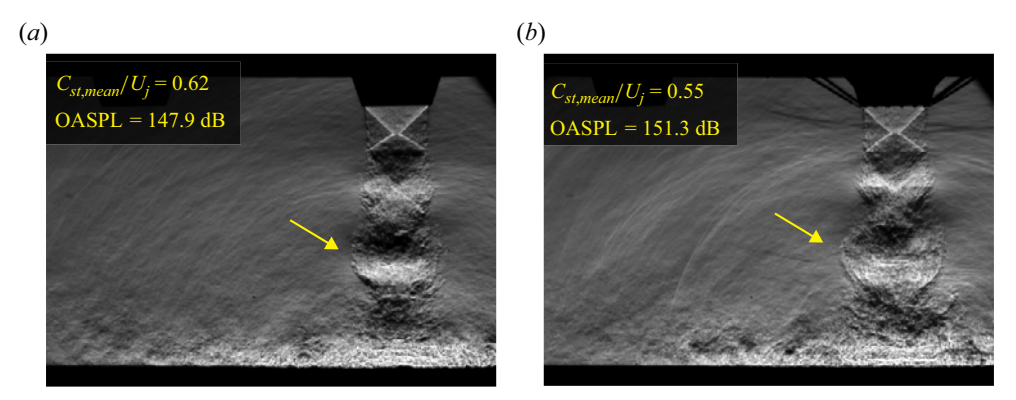


Figure 14. Effect of lift plate on the size of coherent structures for (a) Clean-nozzle and (b) Baseline at H/D = 4.19 (NPR = 3).

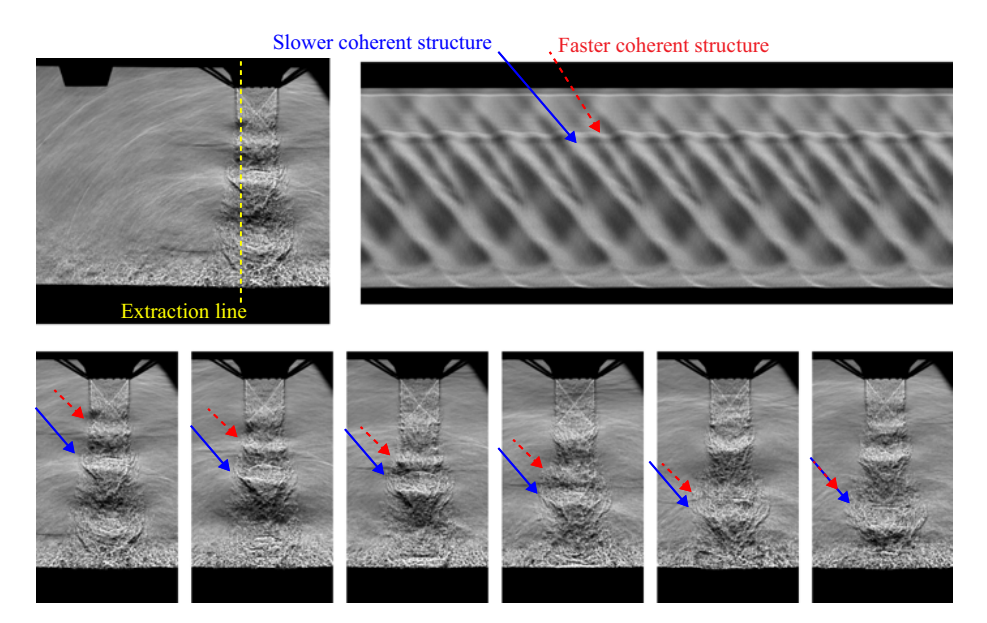


Figure 15. Relation between convection velocity and size of coherent structures at H/D = 5.0 and NPR = 3.67.

of the dominant jet resonance mode. Furthermore, we refer the reader to the detailed investigations by Weightman *et al.* (2019) and Karami & Soria (2021) regarding the impact of nozzle geometry. To clarify, the 'thin-lip' configuration discussed in those studies is not equivalent to the clean-nozzle case in the present study. Instead, their 'thin-lip' condition more closely resembles the baseline configuration used in this work.

An additional analysis was performed to rigorously examine and comprehend any potential relationships among the size and convection velocity of coherent structures and the resonance intensity of a jet. The relationship between the convection velocity and the size of coherent structures can be observed in figure 15. Here, the wave diagram depicts the trajectories of two coherent structures as they convect downstream. The corresponding temporal evolution of the shear-layer instability is depicted in the lower half of figure 15, where each image is temporally displaced by 32 µs from that on its left. One can clearly see a large-scale coherent structure in the middle of the jet column, and another smaller structure is visible upstream of (or above) the larger vortical structure. The sequence of

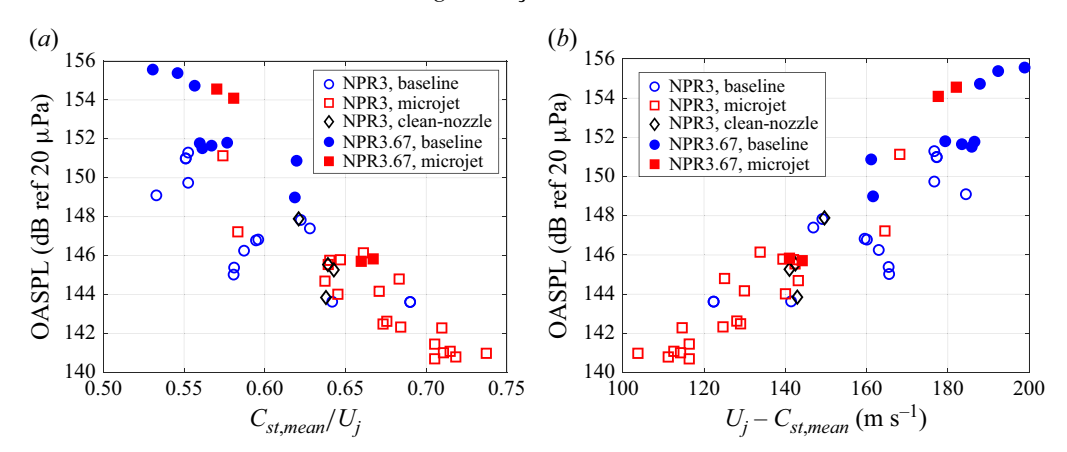


Figure 16. Relation between convection velocity and OASPL (axisymmetric mode only). (a) Convection velocity variation vs. OASPL, (b) Reduction in convection velocity vs. OASPL.

images clearly illustrates how the smaller coherent structure catches up with the larger one, eventually leading to their coalescence into an even larger coherent structure, as seen in the last image. This sequence suggests that smaller coherent structures tend to have higher convection velocities. In addition, the baseline case in figure 14 demonstrates a higher OASPL than the clean-nozzle case, which correlates with the larger size (and slower speed) of its large-scale coherent structures. To ascertain whether a slower coherent structure correlates with a higher OASPL, a distribution of OASPL against the disturbance convection velocity is shown in figure 16(a). Filled symbols represent the ideally expanded (NPR = 3.67) cases and open symbols indicate the overexpanded (NPR = 3) cases. In general, the higher-NPR cases (i.e. NPR = 3.67) tend to have higher OASPL compared to the NPR = 3 cases at a given/fixed normalised convection velocity. More importantly, there is a clear trend of OASPL decreasing as the disturbance convection velocity increases. This confirms that the disturbance convection velocity is indeed associated with OASPL. It is noteworthy that variations in impinging jet configurations lead to changes in disturbance convection velocity, as shown in figure 13. For instance, different external reflective boundary conditions near the nozzle (Weightman et al. 2019), as well as the implementation of multiple impinging jet configurations (Song et al. 2022a), can influence OASPL and are likely to result in alterations to the disturbance convection velocity. As the large-scale coherent structures grow, through entrainment of ambient air, the difference between the fully expanded jet velocity and the disturbance convection velocity may, in a very approximate way, be interpreted as an indication of the shear between them. Hence, this 'one-dimensional shear' could serve as a proxy for the strength of the interaction and the size of the vortical structure. Following this logic, figure 16(b) shows the distribution of OASPL as a function of the reduction in convection velocity $(U_i - C_{st,mean})$. The data from figure 16(a) are replotted, and it more clearly displays the connection between OASPL and convection velocity (or structure size) across different NPR conditions.

5. Effect of the time interval between large-scale coherent structures and reflected acoustic waves

The convection velocity of coherent structures has a minor influence on determining the impingement tonal frequency, as discussed in § 4. This finding suggests that the phase defined in (3.1) varies accordingly. However, this does not provide an explanation for the

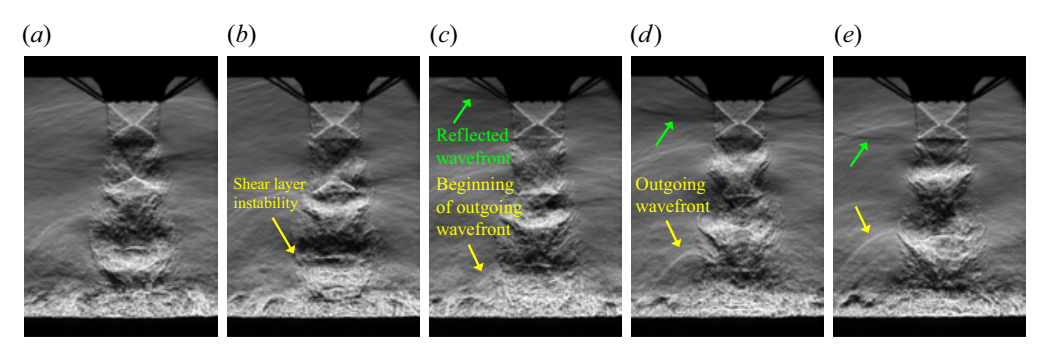


Figure 17. Acoustic wave generation, supersonic nozzle (baseline, NPR = 3, H/D = 4.19). Outgoing wave begins as coherent structure is submerged into the wall-jet region ($\Delta T \approx 32 \,\mu$ s). (a) t = 0, (b) $t = 1 \,\Delta T$, (c) $t = 2 \,\Delta T$, (d) $t = 3 \,\Delta T$ and (e) $t = 4 \,\Delta T$.

nearly independent behaviour of the frequency with respect to the disturbance convection velocity. Instead, this suggests that standing acoustic waves may play a significant role in the nearly constant frequency phenomenon, as the speed of acoustic waves remains relatively constant. Before discussing the standing waves in detail, we first investigate the influence of the reflected acoustic waves, which are a component of the standing acoustic waves. The temporal evolution of a representative flowfield of axisymmetric jet resonance is shown in figure 17, where ΔT ($\approx 32~\mu s$) represents the time interval between successive snapshots of the schlieren visualisation. The impingement of large coherent structures on the ground generates acoustic waves. Meanwhile, a distinct reflected wavefront, as pointed out in figure 17(c), can be observed propagating downstream. Since the reflected acoustic waves may influence the feedback, an analysis is conducted to investigate their potential role in the feedback loop.

The time interval between the arrival of the large-scale coherent structure front and the reflected acoustic wave is measured from the wave diagrams. Figure 18 illustrates the definition of the arrival time interval. The height of the wall-jet boundary is determined by the point of intersection between the front of a coherent structure and the newly generated outgoing acoustic wave. This definition is based on the assumption that there is no delay between the passage of a vortical structure across the stand-off shock (near the wall-jet boundary) and the production of an acoustic wave (Weightman *et al.* 2019). Subsequently, a virtual reflected acoustic wave is drawn from the lower surface of the lift plate, assuming the reflected acoustic wave travels at the same speed as the outgoing acoustic wave and that there is no time delay in the acoustic wave reflection. Again, the time delay, referred to as $\Delta T_{arrival}$, between the reflected acoustic wave and the coherent structure on the wall-jet boundary represents the arrival time interval, as indicated in figure 18.

The distribution of OASPL over the arrival time interval is presented in figure 19. To account for the varying resonance frequencies across different cases, the arrival time is normalised by its corresponding phase period (T_{period}). A normalised arrival time of -0.5 or 0.5 indicates that the reflected wave is out of phase with the newly generated acoustic wave. In other words, the reflected wave arrives in the middle of the arrivals of two consecutive coherent structures. Although the arrival time interval alone cannot fully explain the variation in OASPL, as other factors such as H/D and reflective surface area are involved, it is interesting to note that OASPL tends to increase when the time interval approaches zero. This suggests that the simultaneous arrival of the coherent structure and reflected acoustic wave at the wall-jet boundary (i.e. smaller $\Delta T_{arrival}$) may contribute to the increased OASPL. Additional carefully designed experiments are

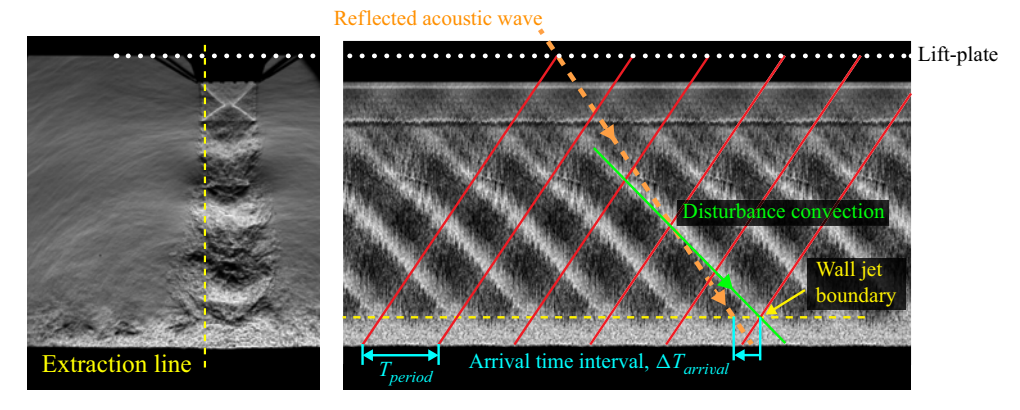


Figure 18. Example of arrival time interval between coherent structure and reflected acoustic wave.

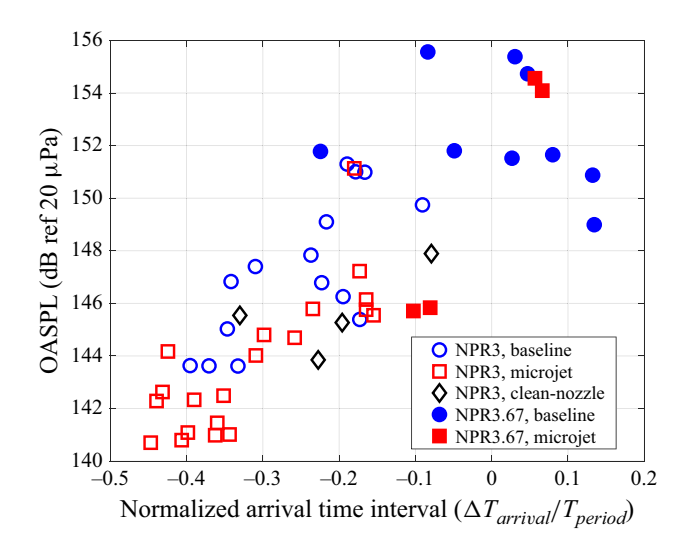


Figure 19. Arrival time interval versus OASPL.

necessary to examine the exact phase/temporal relationship between the arrival of coherent structures and reflected acoustic waves, as well as their effects, including the potential intensification of newly generated acoustic waves. One possible explanation is that the acoustic wave reflected from the lift plate alters the unsteady pressure field around the newly generated acoustic waves, thereby enhancing the intensity. Another possibility is that the downstream-propagating acoustic wave is reflected back – possibly from the wall-jet boundary rather than the ground plate – and coalesces with the newly generated acoustic wave, resulting in amplified acoustic wave generation. In support of the coalescence-based amplification hypothesis, schlieren (density gradient) images indicate potential density differences across the wall-jet boundary. The acoustic impedance mismatch between the wall-jet and the ambient region leads to partial reflection of acoustic waves from the wall-jet boundary. Nevertheless, further investigation is necessary to fully understand this mechanism.

Figure 20 shows the distribution of the arrival time interval across various impingement distances, with dashed ellipses encompassing data points within the same stage. For the overexpanded conditions in figure 20(a), the time arrival range is biased towards negative

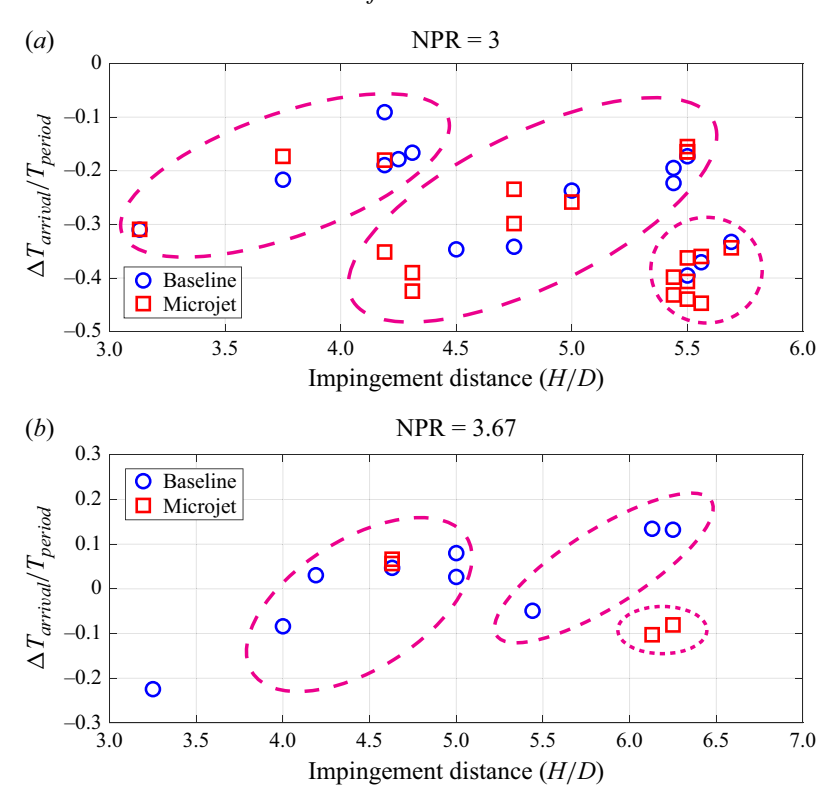


Figure 20. Variation of the arrival time interval over impingement distances at (a) NPR = 3 and (b) NPR = 3.67. Dashed ellipses encircle the same stage.

time intervals. By contrast, in the ideally expanded jet case shown in figure 20(b), the time arrival range does not display as much skewness as observed in the overexpanded case. Despite the differences in disturbance convection velocity between the baseline and microjet cases, as seen in figures 12 and 13, there is an overlap in the time intervals between the two cases. This suggests that these time intervals are not particularly affected by the disturbance convection velocity. Furthermore, as the impingement distance increases, the arrival time interval tends to increase, but it abruptly decreases when a stage shift occurs. This dynamic may explain the staging behaviour triggered by microjet activation, observed near NPR = 3 and H/D = 4.2 in figure 12. When a microjet is activated, it increases the disturbance convection velocity by inhibiting the growth of coherent structures. Consequently, the disturbance convection velocity accelerates, leading to a stage shift when the time interval exceeds -0.1, which is not supported as shown in figure 20(a).

6. Standing waves and acoustic speed-based frequency model

Standing waves are investigated since convection velocities do not have a strong impact on the impingement tonal frequency, which remains nearly constant. To analyse standing waves, the standard deviation of the flow field is used, following the approach of previous research (Panda 1999; Edgington-Mitchell, Honnery & Soria 2015). Figure 21 displays the standard deviations of the schlieren image sets at selected impingement distances. The left-hand column of figure 21 displays the standard deviation fields at H/D = 4.19 and 5, with

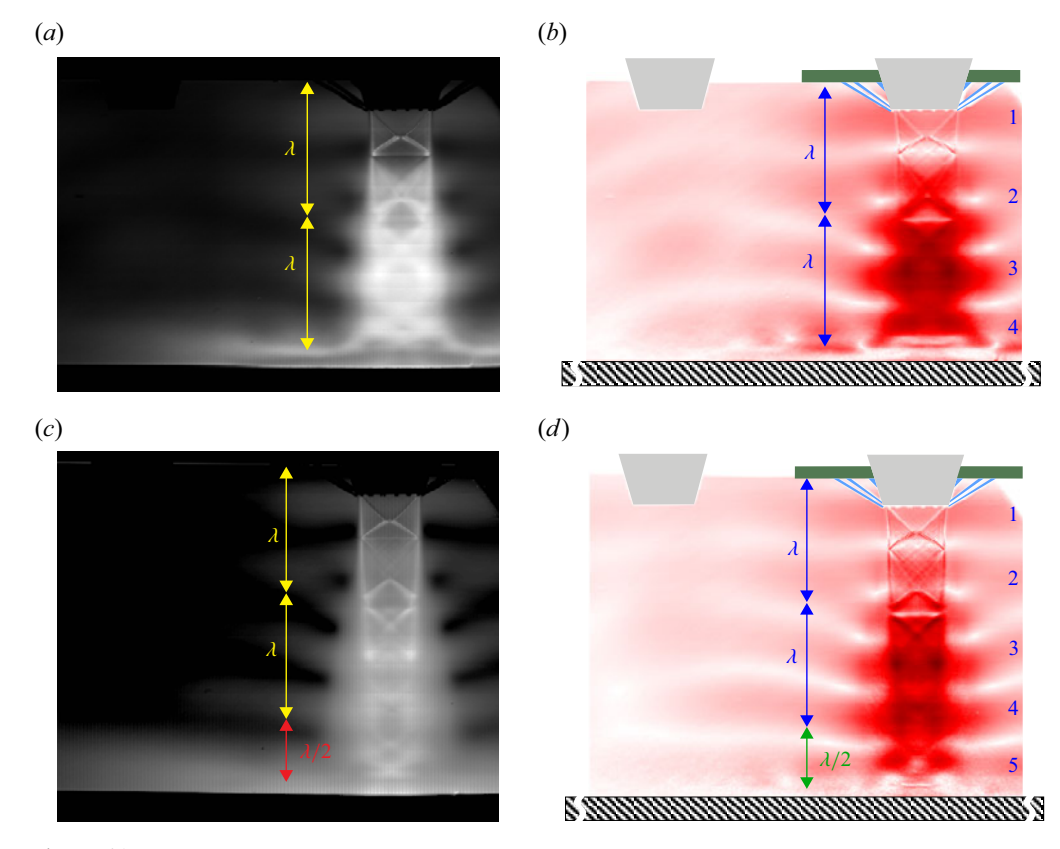


Figure 21. Acoustic standing-wave patterns for NPR = 3. (a) Standard deviation field at H/D = 4.19, (b) Magnitude field (|v|) of total DMD, H/D = 4.19, (c) Standard deviation field at H/D = 5 and (d) Magnitude field (|v|) of total DMD, H/D = 5.

the greyscale adjusted to highlight the standing-wave pattern. In the right-hand column, the magnitude fields of the total DMD mode corresponding to the impingement tonal frequency provide a clearer visualisation of the standing-wave pattern. The magnitude field $(|v_j|)$ is proportional to the standard deviation field of a mode related to a certain frequency. The DMD decomposes a kth schlieren image, x_k , based on discrete frequencies as

$$x_k \approx A^k x_0 \approx \sum_{j=1}^r v_j \Lambda_{DMD,j}^k \alpha_j = \sum_{j=1}^r v_j e^{\omega_j t} \alpha_j = \sum_{j=1}^r |v_j| e^{i\phi_{v_j}} e^{(\omega_{j,real} + i\omega_{j,imag})t} \alpha_j, \quad (6.1)$$

where A represents a linear mapping matrix for the subsequent flowfield in the following snapshot $(x_{k+1} = Ax_k)$ (Schmid 2010). Dynamic mode is decomposed by eigenvalue decomposition of A in (6.1). Here $\Lambda_{DMD,j}$ represents the temporal dynamics (i.e. frequency, growth/decay) of the mode number (j), v and α stand for the spatial mode and mode amplitude, respectively, α_j is a scalar value and the time evolution term is sinusoidal, and if $\omega_{j,real}$ is assumed to be zero since the impingement tone is almost pure oscillation, then σ (DMD mode $_j(t)$) = $|v_j||\alpha_j|/\sqrt{2}$. The total DMD method is employed in this study as it offers improved mode extraction for noisy datasets compared with standard DMD (Hemati $et\ al.\ 2017$). A detailed methodology of the total DMD calculation used in this study can be found in the work by Song $et\ al.\ (2022b)$.

The length of the arrows in figure 21 represents the wavelength ($\lambda = C_a/f_{impinging}$) of the outgoing acoustic waves, which is calculated using the impingement tone frequency obtained from microphone measurements. The tip of the top arrow is positioned at the lower surface of the lift plate, while the bottom tip of the arrows extends towards the wall-jet boundary. As seen here, the length of the arrow approximately corresponds to the wavelength of the standing wave (i.e. the length of two lobes). The impingement tonal frequency undergoes a stage jump between H/D = 4.19 and 5 – specifically around H/D = 4.4 (see figure 12) – with the standing wave exhibiting four lobes for H/D = 4.19 and five lobes for H/D = 5. At H/D = 4.19, it takes four cycles (= N_{stage}) for an acoustic wave to complete a round trip between the wall-jet boundary and lift plate, whereas at H/D = 5, it requires five cycles (= N_{stage}). Therefore, the number of lobes between the lower surface of the lift plate and the wall-jet boundary corresponds to the number of cycles needed for a round trip, and it increases as staging occurs.

As pointed out earlier, excluding staging behaviour, it has been demonstrated that variations in convection velocity due to changes in NPR (figure 10a) or microjet activation (figure 12) have a negligible effect on the impingement tonal frequency. This implies that the disturbance convection velocity alone is not the dominant factor in determining the impingement frequency. This raises the question of whether the impingement tonal frequency model needs to include a convection velocity term for frequency prediction, especially in the presence of strong standing acoustic waves, even though large-scale coherent structures are directly associated with the generation of acoustic waves. A staging jump is observed alongside a change in the number of the acoustic standingwave lobes between the lift plate and wall-jet boundary. This points towards the likelihood of the acoustic standing wave having a key role in defining the impingement frequency. Additionally, the reflected acoustic wave contributes to the formation of the acoustic standing wave and exhibits a relationship with the large-scale coherent structure in terms of arrival time at the wall-jet boundary, as observed in figure 20. Thus, it is proposed to replace the downstream convection velocity term in (3.1) with the speed of sound when strong acoustic standing waves are present between the lift plate and the impingement plate. This revision yields (6.2), which is referred to as an acoustic-base model:

$$f_{impinging} = \frac{N_a + P_a}{2(H + L_{gap})/C_a}. (6.2)$$

The phase (P) and N_{stage} have been redefined as P_a and N_a , respectively. Here N_a is equivalent to the number of standing-wave lobes present between the lift plate and the wall-jet boundary. The detailed explanation of the phase lead/lag is discussed later with the help of wave diagrams.

For the baseline case at NPR of 3, the simplified frequency formulation (3.1) and acoustic speed-based frequency model (6.2) are presented as dotted lines on top of the same acoustic spectrogram in figure 22. It is worth noting that the Strouhal number near 0.33 corresponds to a non-axisymmetric mode, which is not the primary focus of the present study, as aforementioned. This is because, at high impingement distances, the frequency of the non-axisymmetric mode, which originates near the third shock cell (Liu et al. 2021) and is associated with the screech tone (Song et al. 2021), is not significantly influenced by impingement distance.

For the calculation of the simplified frequency formulation (3.1) shown in figure 22(a), the disturbance convection velocity (218 m s⁻¹) and phase lead/lag (0.43) values obtained at an impingement distance of 4.19 are applied as constants over the entire range of impingement distances. The $N_{stage} = 5$ line exhibits a close alignment with the measured impingement tone frequencies, represented by dark stripes in the range 0.4 < St < 0.5; this

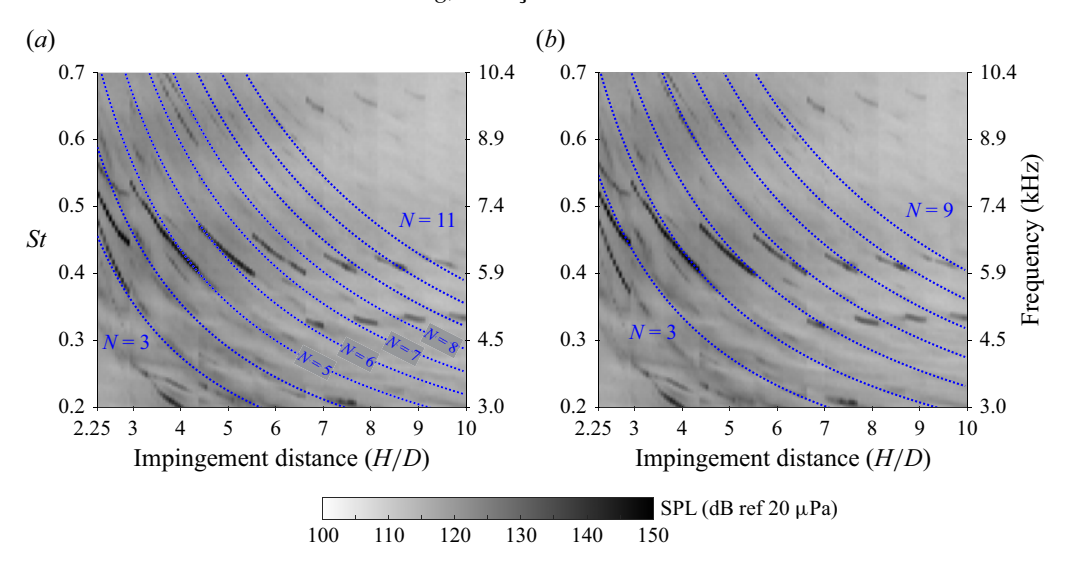


Figure 22. Comparison between frequency formulations for baseline case at NPR = 3. (a) Simplified formulation ((3.1), using P = 0.43, $C_{st,mean} = 218 \text{ m s}^{-1}$) and (b) Acoustic base formulation ((6.2), using $P_a = 0.33$).

resonance occurring within the 0.4 < St < 0.5 range is associated with the axisymmetric mode. This alignment is expected since the $N_{stage} = 5$ line is calculated based on the impingement tone measurement at H/D = 4.19. However, as the impingement distance increases, the $N_{stage} = 7$ and 8 lines do not match with the measured impingement tones. As the impingement distance increases even further, the alignment is once again observed for the $N_{stage} = 9$ to 11 lines. This observed matching trend is due to the calculated frequency lines being closer to each other than the actual impingement tones. The point is not to imply that the physical meaning of Powell's formulation (1.1) is incorrect, but rather to underscore the fact that (1.1) is difficult to use in its stated form for the purpose of frequency prediction since the mean convection velocity and phase (P) both change with impingement distance.

As an alternative, the acoustic speed-based model results from (6.2) are depicted in figure 22(b). For the calculation, $N_a = 4$ and $P_a = 0.33$, which are based on the impingement tone at H/D = 4.19, are applied across the entire range of impingement distances. The calculated frequency lines closely align with the measured impingement tones, and the spacing between the frequency lines matches that of the measured impingement tones. Even without considering the disturbance convection velocity, replacing it with the acoustic wave speed improves agreement with the measured impingement tones within the range of 0.4 < St < 0.5.

6.1. Phase lead/lag and N_{stage} in wave diagram

The acoustic speed-based model, (6.2), can be formulated with a time delay term instead of the phase as

$$f_{impinging} = \frac{N_a}{2(H + L_{gap})/C_a + T_{delay,a}}.$$
(6.3)

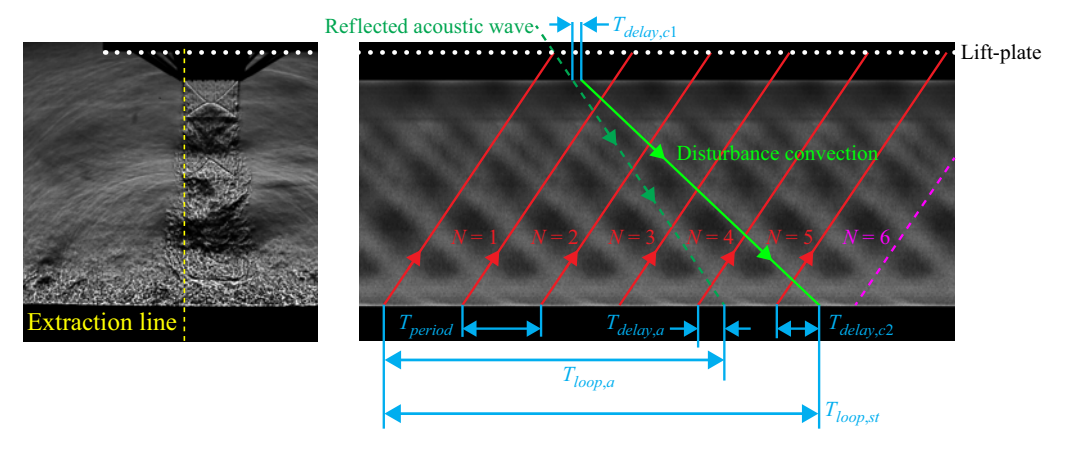


Figure 23. Phase and time delay relation. Jet is operated at NPR = 3 and H/D = 4.19.

Upon equating (6.3) with (6.2), the phase (P_a) can be expressed in terms of the time delay (T_{delay}) and the period of the impingement tone (T_{period}) as

$$P_a = N_a \frac{-T_{delay,a}}{2(H + L_{gap})/C_a + T_{delay,a}} = \frac{-T_{delay,a}}{T_{period}}.$$
 (6.4)

The two time variables (T_{delay} , T_{period}) can be identified in a wave diagram, as shown in an example depicted in figure 23. Here, the upstream-propagating acoustic waves are highlighted with red solid lines. The horizontal spacing between these acoustic lines corresponds to the period of the impingement tonal frequency ($T_{period} = 1/f_{impinging}$). For an acoustic wave (e.g. the leftmost red solid line), it originates near the ground plate and is reflected back at the lower surface of the lift plate, as represented by the dotted line. The wave completes one loop of travel when it returns to the ground plate, with a duration of $T_{loop,a}$ (= $2(H + L_{gap})/C_a$). Over the loop period ($T_{loop,a}$), four cycles of the impingement tone period (T_{period}) are completed, and this also corresponds to the number of standing-wave lobes, as observed in figure 21(b).

In the simplified model (3.1), there are two time delays that need to be taken into account, as shown in figure 23: $T_{delay,c1}$, which represents the delay between the generation of the coherent structure from the reflected acoustic wave, and $T_{delay,c2}$, which denotes the time delay between the coherent structure and the acoustic wave. Consequently, the frequency in (3.2) can be expressed in terms of these two time delays instead of the phase (*P*). Thus, the frequency in (3.2) can be expressed using the two time delays instead of the phase as

$$f_{impinging} = \frac{N_{stage}}{\frac{H + 2L_{gap}}{C_a} + \frac{H}{C_{st,mean}} + T_{delay,cI} + T_{delay,c2}}.$$
 (6.5)

By equating (6.5) and (3.2), the phase (P) can be expressed in terms of the time variables as

$$P = -(T_{delay,c1} + T_{delay,c2})/T_{period}.$$
(6.6)

A positive phase value (P) indicates a phase lead, which means the total delay time is negative. The phase values calculated from the microphone measurements and wave diagrams are presented in table 2. It should be noted that phase values obtained from the wave diagrams are expected to be identical to those derived from the microphone

Phase	Stage	Phase from microphone	Phase from wave diagram
P_a	$N_a = 4$	0.332 (from (6.2))	$-T_{delay,a}/T_{period}$ = -(-53.8) \(\mu s/161.4\)\(\mu s = 0.333\)
P	$N_{stage} = 5$	0.433 (from (3.2))	$-(T_{delay,c1} + T_{delay,c2})/T_{period}$ = -(18.2 - 86.9) \(\mu s'\)161.4 \(\mu s = 0.426\)

Table 2. Comparison of phase values obtained from microphone measurements and time delays in wave diagram.

data, as the wave diagrams are constructed based on the tonal frequency measured by the microphone. The emphasis is not on highlighting the agreement of phase values, but rather on verifying the meaning of the phase value in terms of the time delay.

The loop period $(T_{loop,st} = (N_{stage} + P)T_{period})$ in the simplified frequency formulation (3.1) is $5.43T_{period}$. The range of the phase value (-1 < P < 1) allows for selection of N_{stage} as either 5 or 6. However, in the present study, N_{stage} is chosen as 5 since the sixth cycle above the wall-jet boundary, as seen in figure 23, falls outside of the loop period. Note that N_{cycle} in figure 23 is the number of cycles rather than denoting a specific acoustic wave. Similarly, for the acoustic speed-based model (6.2), N_a is chosen as 4 for the same reason.

6.2. Frequency range from vortex-sheet model and validation of acoustic speed-based model

Both impingement frequency formulations ((3.2) and (6.2)) describe the behaviour of impingement tonal frequencies. However, they do not predict a specific impingement tonal frequency, as they do not define a frequency range. Here, we use the vortex-sheet model (Tam & Ahuja 1990) to examine the range of impingement tonal frequencies. The mathematical expression for the vortex-sheet model, as given in (16) of the work by Tam & Ahuja (1990), is

$$|\xi_{+}| J_{n}(|\xi_{-}\alpha|) \frac{K_{n-1}(|\xi_{+}\alpha|) + K_{n+1}(|\xi_{+}\alpha|)}{K_{n}(|\xi_{+}\alpha|)} + \frac{C^{2} |\xi_{-}|}{(a_{\infty}C/a_{j} - M_{j})^{2}} [J_{n-1}(|\xi_{-}\alpha|) - J_{n+1}(|\xi_{-}\alpha|)] = 0,$$
(6.7)

where J_n and K_n are the *n*th-order Bessel function of the first kind and modified Bessel function, respectively. The solutions of (6.7) for the axisymmetric mode (n = 0) at NPRs of 3 and 3.67 are shown in figure 24. These solutions represent the dispersion relation of the neutral wave. The frequency ranges exhibiting negative group velocity (dSt/dk) of the neutral waves are shaded in pink and labelled as $A1, A2, \ldots, A(m)$ above each shaded area. The shaded regions indicate the allowable frequency ranges in which the shear-layer instability is excited by upstream-propagating neutral waves (Bogey & Gojon 2017). The dashed lines stand for upstream wave propagation at the speed of sound, and the circle symbols indicate when the solution of (6.7) approaches the speed of sound (i.e. the dashed line). Note that the lower limit of the shaded areas (represented by circles) for the axisymmetric mode in figure 24 can be easily calculated using (6.8) (originally presented as (22) in the work by Tam & Ahuja (1990)):

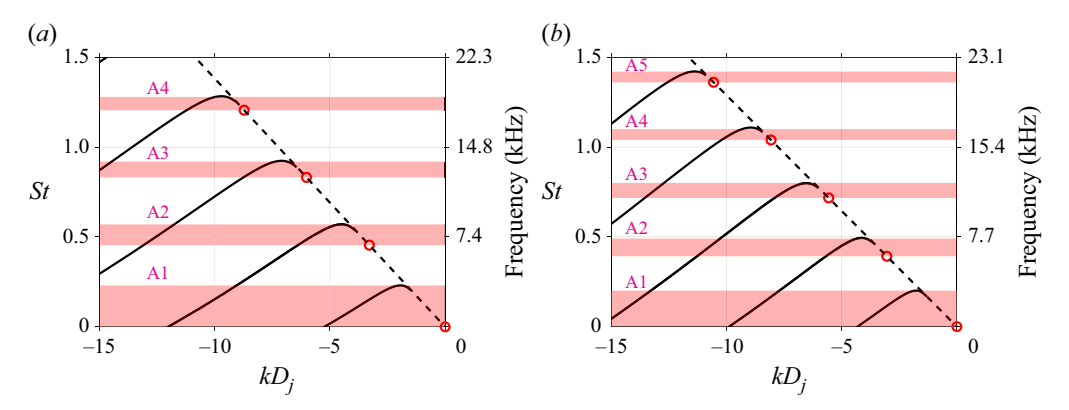


Figure 24. Dispersion relation of neutral waves from the vortex-sheet model. Here k denotes the wavenumber. (a) Axisymmetry mode (n = 0) at NPR = 3 and (b) Axisymmetry mode (n = 0) at NPR = 3.67.

$$St = \frac{fD_j}{U_j} = \frac{1}{\pi} \frac{\omega R_j}{U_j} \to \frac{\text{Roots of } J_1}{\pi M_j (a_j / a_\infty) \left[(a_\infty / a_j + M_j)^2 - 1 \right]^{1/2}}$$
 (Roots of $J_1 \approx 3.83, 7.02, \dots$), (6.8)

where M_j is fully expanded jet Mach number, a_j and a_∞ denote the speed of sound inside and outside the jet, respectively.

On the acoustic spectrograms shown in figure 25, the allowable frequency ranges are indicated by shaded regions for the clean-nozzle case at NPRs of 3 and 3.67. It is worth noting that the impingement tones near St = 0.5 for NPR = 3 and St = 0.4 for NPR = 3.67 correspond to the axisymmetric mode, while the tones near St = 0.35 for NPR = 3 represent the non-axisymmetric mode (highlighted within a dotted box). In both cases of NPR, the allowable frequency ranges of A2 exhibit a slight overestimation of the impingement tonal frequency range. This marginal overestimation might be attributed to the absence of modelling of the thickness of the jet mixing layer (Tam & Ahuja 1990). Nevertheless, the vortex-sheet model offers an excellent approximation of the measured frequency range. The frequency line, depicted by dotted lines in figure 25, is computed using (6.2), where the phase (P_a) of 0.33 is obtained from the baseline condition. Additionally, the gap length (L_{gap}) is assumed to be zero, as the lift plate is not installed (i.e. acoustic reflection occurs at the nozzle lip). It is noteworthy that the dotted frequency lines in figures 25(a) and 25(b) are identical in the frequency scale (but not in St). By combining these calculated frequency lines with the frequency range of A2, it becomes possible to narrow down the scope of prediction for the impingement tonal frequencies.

Similarly, figure 26 shows acoustic spectrograms for the baseline case, and the blue dotted lines represent frequencies calculated from the acoustic speed-based model (6.2) with P_a of 0.33 and L_{gap} of 0.53D. The dotted lines in the frequency scale are the same across different NPR conditions in figure 26 (not in the St scale). In the case of NPR = 3.67 and 4.5, as seen in figures 26(b) and 26(c), the impingement tones near St = 0.6, highlighted by the white dashed ellipses, correspond to the axisymmetric mode. The allowable frequency range, derived from the vortex-sheet model, is emphasised with shades in pink on the acoustic spectrograms. Note that impingement tones near the A2 bands are also associated with the axisymmetric mode. The frequency (blue dotted) lines agree well with the measured impingement tones near/below the A2 allowable frequency band. In all three NPR cases, the measured impingement tonal frequencies, related to

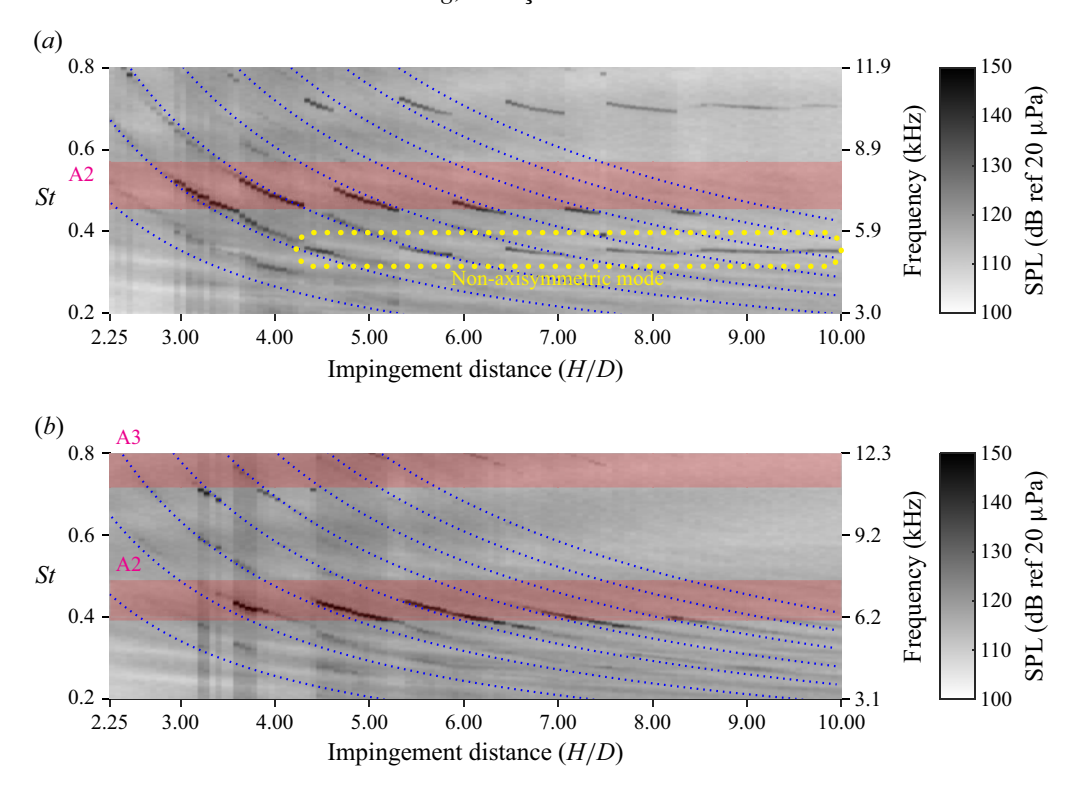


Figure 25. Acoustic spectrograms for the clean-nozzle case at (a) Overexpanded, NPR = 3 and (b) Ideally expanded, NPR = 3.67. Blue dotted lines represent frequencies calculated from the acoustic speed-based model (6.2). Shaded areas A2 and A3 indicate the allowable frequency range from the vortex-sheet model, as discussed in figure 24.

the axisymmetric mode, are near/below the lower boundary of the allowable frequency ranges (A2 and A3). Nevertheless, the allowable frequency ranges provide a good first estimation for predicting the impingement tonal frequency when used with the acoustic speed-based model. The modest disagreement of the allowable frequency ranges arises from the presence of the lift plate positioned behind the nozzle exit, which modifies the feedback loop; the acoustic wave's travel distance is extended by $2L_{gap}$, and consequently, the impingement frequency decreases. It should be noted that the allowable St ranges (i.e. A2 and A3 bands) are identical to those in the clean-nozzle cases in figure 25 for corresponding NPR conditions. Although the presence of a lift plate changes the feedback loop, the different reflection location, from the perspective of the neutral wave, introduces a time delay rather than a frequency change since the upstream-propagating neutral waves are neither unstable nor damped (Tam & Ahuja 1990) (which are inherent characteristics of the jet itself); the neutral wave is not necessarily acoustic since the A1 and A2 upstream-propagating neutral waves are not free-stream acoustic wave in free-jet flows (Edgington-Mitchell *et al.* 2018). A possible explanation for this disagreement is that neutral waves initiate instabilities in the jet shear layer, resulting in closure of the feedback loop through the ambient acoustic waves, rather than the neutral wave itself.

For the case of NPR = 3, the tones near St = 0.33 associated with the non-axisymmetric mode are indicated by the yellow dotted box in figure 26(a). For the case at NPR of 4.5 in figure 26(c), the impingement tonal frequencies associated with the non-axisymmetric mode near St = 0.5 are noticeably more influenced by impingement distance than tones

2.25

3.00

4.00

5.00

Journal of Fluid Mechanics

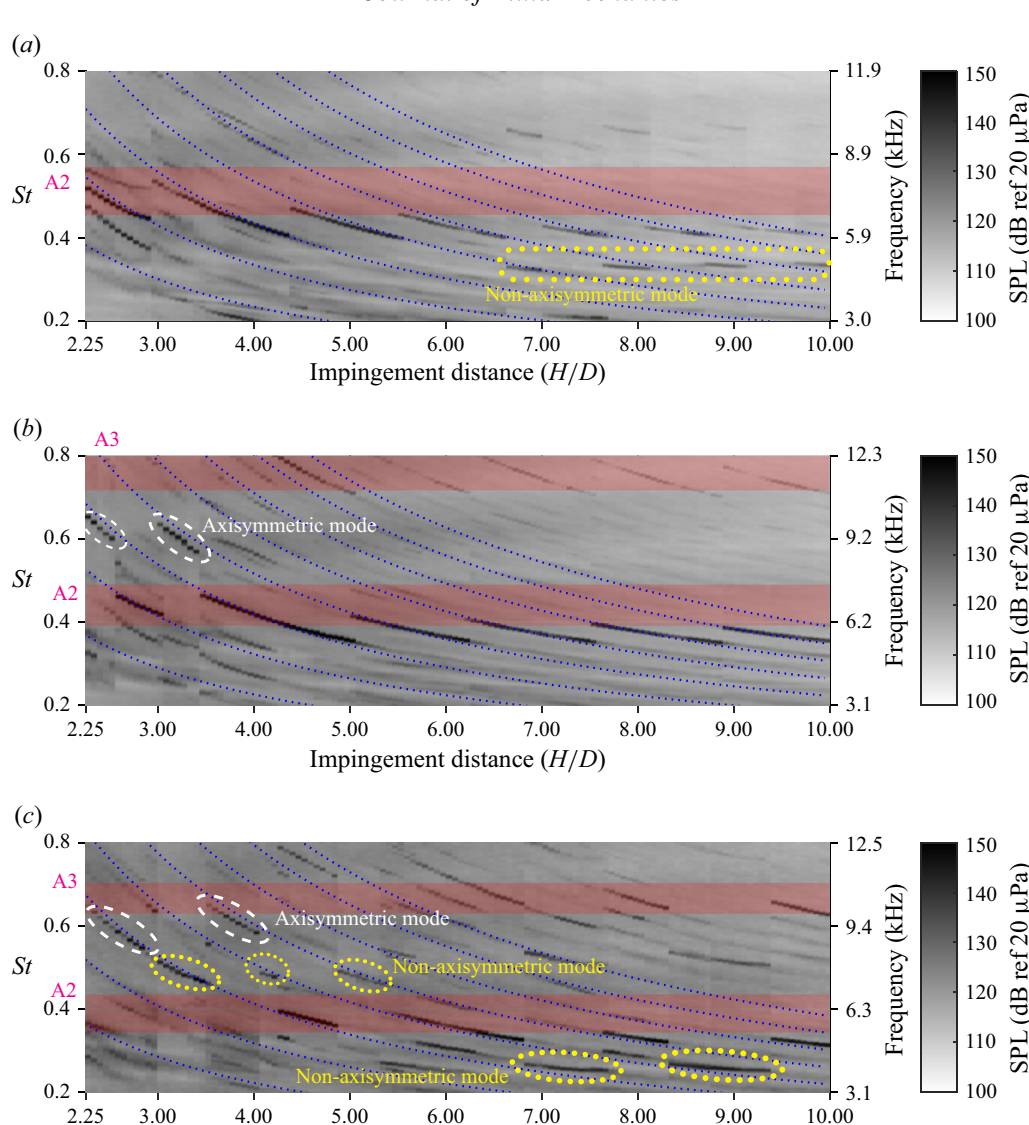


Figure 26. Acoustic spectrograms for baseline case at (a) Overexpanded, NPR = 3, (b) Ideally expanded, NPR = 3.67 and (c) Underexpanded, NPR = 4.50. Blue dotted lines represent frequencies calculated from the acoustic speed-based model (6.2). Shaded areas A2 and A3 indicate the allowable frequency range from the vortex-sheet model, as discussed in figure 24.

Impingement distance (H/D)

7.00

8.00

9.00

10.00

near St = 0.25. This distinction can be explained by different source locations of the nonaxisymmetric mode, as it can be generated near either the wall-jet area or the third shock cell (Liu et al. 2021), such that the tones near St = 0.5 exhibit a stronger dependence on the impingement distance.

The acoustic speed-based model holds the advantage of not relying on the convection velocity of disturbances, which exhibits dependence on impingement distance, NPR and microjet activation status. Although the acoustic speed-based model demonstrates good agreement with experimental observations, it has certain limitations, such as the absence of impingement tones, non-axisymmetric mode and staging behaviour. Furthermore,

agreement with experimental results suggests that acoustic standing waves may play an important role in the feedback loop, consisting of downstream-travelling coherent structures and upstream-propagating acoustic waves.

7. Conclusions

The role of disturbance convection velocity in the resonance of a supersonic impinging jet has been investigated through acoustic measurements and high-speed schlieren flow visualisations. To construct wave diagrams at several impingement distances, a phase-bin-averaging method is applied to the schlieren image sets with the assistance of acoustic measurements. The convection velocities are then determined from the wave diagrams for both over- and ideally expanded jet conditions. The conclusions derived from this study are as follows:

- (i) A larger reflection surface extends the NPR range of the nearly constant impingement tonal frequency. A parametric study was performed to investigate a relationship between disturbance convection velocity and resonance frequency. A higher NPR increases disturbance convection velocity; however, the phase lead/lag value needs to be changed to keep the tonal frequency nearly constant.
- (ii) The mean convection velocity of large-scale coherent structures is influenced by various factors such as the impingement distance and other conditions. For instance, the activation of microjets can increase the disturbance convection velocity. While the impact of disturbance convection velocity on the impingement tonal frequency is generally minimal, it can result in a stage jump. Furthermore, the disturbance convection velocity can be varied by the external reflective boundary condition near the nozzle. It is observed that when the size of the large-scale coherent structure is larger, the convection velocity tends to be slower, thereby generating stronger noise.
- (iii) The time interval between the arrival of the reflected acoustic waves and the large-scale coherent structures at the wall-jet boundary potentially influences the OASPL, and the role of the reflected acoustic waves in this relationship is hypothesised.
- (iv) Acoustic standing waves form between the lower surface of the lift plate and the wall-jet boundary. Based on the presence of standing waves and the limited influence of disturbance convection velocity on impingement tonal frequency, an acoustic speed-based model to estimate impingement tonal frequency is proposed. The allowable frequency range for the axisymmetric mode is calculated using the vortex-sheet model, which demonstrates good agreement with the impingement tonal frequency observed under the clean-nozzle condition. By combining the acoustic speed-based model with the vortex-sheet model, it becomes feasible to predict impingement tonal frequencies associated with the axisymmetric mode.

Supplementary movies. Supplementary movies are available at https://doi.org/10.1017/jfm.2025.10688.

Funding. This research was supported by the Office of Naval Research. Partial support was provided by NSF, AFOSR, FCAAP, FAMU-FSU College of Engineering and Don Fuqua Eminent Scholar Fund.

Declaration of interests. The authors report no conflict of interest.

REFERENCES

ALVI, F.S., LADD, J.A. & BOWER, W.W. 2002 Experimental and computational investigation of supersonic impinging jets. AIAA J. 40 (4), 599–609.

- ALVI, F.S., LOU, H., SHIH, C. & KUMAR, R. 2008 Experimental study of physical mechanisms in the control of supersonic impinging jets using microjets. *J. Fluid Mech.* **613**, 55–83.
- ALVI, F.S., SHIH, C., ELAVARASAN, R., GARG, G. & KROTHAPALLI, A. 2003 Control of supersonic impinging jet flows using supersonic microjets. *AIAA J.* 41 (7), 1347–1355.
- ARAKERI, V.H., KROTHAPALLI, A., SIDDAVARAM, V., ALKISLAR, M.B. & LOURENCO, L.M. 2003 On the use of microjets to suppress turbulence in a Mach 0.9 axisymmetric jet. *J. Fluid Mech.* **490**, 75–98.
- BOGEY, C. & BAILLY, C. 2010 Influence of nozzle-exit boundary-layer conditions on the flow and acoustic fields of initially laminar jets. *J. Fluid Mech.* **663**, 507–538.
- BOGEY, C. & GOJON, R. 2017 Feedback loop and upwind-propagating waves in ideally expanded supersonic impinging round jets. J. Fluid Mech. 823, 562–591.
- BRÈS, G.A., JORDAN, P., JAUNET, V., LE RALLIC, M., CAVALIERI, A.V.G., TOWNE, A., LELE, S.K., COLONIUS, T. & SCHMIDT, O.T. 2018 Importance of the nozzle-exit boundary-layer state in subsonic turbulent jets. J. Fluid Mech. 851, 83–124.
- CHATTERJEE, A. 2000 An introduction to the proper orthogonal decomposition. Curr. Sci. 78 (7), 808-817.
- EDGINGTON-MITCHELL, D. 2019 Aeroacoustic resonance and self-excitation in screeching and impinging supersonic jets a review. *Intl J. Aeroacoust.* 18, 118–188.
- EDGINGTON-MITCHELL, D., HONNERY, D.R. & SORIA, J. 2015 Staging behaviour in screeching elliptical jets. *Intl J. Aeroacoust.* **14** (7), 1005–1024.
- EDGINGTON-MITCHELL, D., JAUNET, V., JORDAN, P., TOWNE, A., SORIA, J. & HONNERY, D. 2018 Upstream-travelling acoustic jet modes as a closure mechanism for screech. *J. Fluid Mech.* 855, R1.
- EDGINGTON-MITCHELL, D., LI, X., LIU, N., HE, F., WONG, T.Y., MACKENZIE, J. & NOGUEIRA, P. 2022 A unifying theory of jet screech. *J. Fluid Mech.* **945**, A8.
- FIORE, M., PARISOT-DUPUIS, H., ETCHEBARNE, B. & GOJON, R. 2022 Spectral proper orthogonal decomposition of coupled hydrodynamic and acoustic fields: application to impinging jet configurations. *Comput. Fluids* 241, 105484.
- HEMATI, M.S., ROWLEY, C.W., DEEM, E.A. & CATTAFESTA, L.N. 2017 De-biasing the dynamic mode decomposition for applied koopman spectral analysis of noisy datasets. *Theor. Comput. Fluid Dyn.* **31** (4), 349–368.
- JAUNET, V., MANCINELLI, M., JORDAN, P., TOWNE, A., EDGINGTON-MITCHELL, D., LEHNASCH, G. & GIRARD, S. 2019 Dynamics of round jet impingement. 25th AIAA/CEAS Aeroacoustics Conference. AIAA Paper 2019-2769.
- JORDAN, P. & COLONIUS, T. 2013 Wave packets and turbulent jet noise. Annu. Rev. Fluid Mech. 45 (1), 173–195.
- KARAMI, S. & SORIA, J. 2018 Analysis of coherent structures in an under-expanded supersonic impinging jet using spectral proper orthogonal decomposition (SPOD). *Aerospace* 5 (3), 73.
- KARAMI, S. & SORIA, J. 2021 Influence of nozzle external geometry on wavepackets in under-expanded supersonic impinging jets. J. Fluid Mech. 929, A20.
- KNAST, T., BELL, G., WONG, M., LEB, C.M., SORIA, J., HONNERY, D.R. & EDGINGTON-MITCHELL, D. 2018 Coupling modes of an underexpanded twin axisymmetric jet. *AIAA J.* **56** (9), 3524–3535.
- Krothapalli, A., Rajkuperan, E., Alvi, F.S. & Lourenco, L. 1999 Flow field and noise characteristics of a supersonic impinging jet. *J. Fluid Mech.* 392, 155–181.
- LESSHAFFT, L., SEMERARO, O., JAUNET, V., CAVALIERI, A.V.G. & JORDAN, P. 2019 Resolvent-based modeling of coherent wave packets in a turbulent jet. *Phys. Rev. Fluids* 4 (6), 063901.
- LIU, N., LI, X., HAO, P., ZHANG, X. & HE, F. 2021 Mode switch in tonal under-expanded impinging jets. *Phys. Fluids* **33** (12), 124102.
- NOBACH, H. & HONKANEN, M. 2005 Two-dimensional gaussian regression for sub-pixel displacement estimation in particle image velocimetry or particle position estimation in particle tracking velocimetry. *Exp. Fluids* **38** (4), 511–515.
- NOGUEIRA, P.A.S., CAVALIERI, A.V.G., MARTINI, E., TOWNE, A., JORDAN, P. & EDGINGTON-MITCHELL, D. 2024 Guided-jet waves. *J. Fluid Mech.* 999, A47.
- PANDA, J. 1999 An experimental investigation of screech noise generation. J. Fluid Mech. 378, 71–96.
- POWELL, A. 1988 The sound-producing oscillations of round underexpanded jets impinging on normal plates. J. Acoust. Soc. Am. 83 (2), 515–533.
- SCHMID, P.J. 2010 Dynamic mode decomposition of numerical and experimental data. *J. Fluid Mech.* **656**, 5–28.
- SCHMIDT, O.T. & COLONIUS, T. 2020 Guide to spectral proper orthogonal decomposition. AIAA J. 58 (3), 1023–1033.

M. Song, S. Seçkin and F.S. Alvi

- SCHMIDT, O.T., TOWNE, A., COLONIUS, T., CAVALIERI, A.V.G., JORDAN, P. & BRÈS, G.A. 2017 Wavepackets and trapped acoustic modes in a turbulent jet: coherent structure eduction and global stability. *J. Fluid Mech.* **825**, 1153–1181.
- SCHMIDT, O.T., TOWNE, A., RIGAS, G., COLONIUS, T. & BRÈS, G.A. 2018 Spectral analysis of jet turbulence. *J. Fluid Mech.* **855**, 953–982.
- SINHA, A., RODRÍGUEZ, D., BRÈS, G.A. & COLONIUS, T. 2014 Wavepacket models for supersonic jet noise. J. Fluid Mech. 742, 71–95.
- SONG, M. 2024 Dynamics of single and dual supersonic impinging jets and response to adaptive microjetdriven control. *PhD thesis*, The Florida State University, Tallahassee, Florida.
- SONG, M., BHARGAV, V.N., SEÇKİN, S., SELLAPPAN, P., KUMAR, R. & ALVI, F.S. 2021 Active flow control of single and dual supersonic impinging jets using microjets. AIAA Scitech 2021 Forum. *AIAA Paper* 2021-1637.
- SONG, M., BHARGAV, V.N., SEÇKİN, S., SELLAPPAN, P., KUMAR, R. & ALVI, F.S. 2022a Dynamics and response to control of single and dual supersonic impinging jets. AIAA J. 60 (5), 2860–2876.
- SONG, M., SEÇKİN, S., BHARGAV, V.N., SELLAPPAN, P., KUMAR, R. & ALVI, F.S. 2022b Dynamics and response to microjet control of dual supersonic impinging jets. AIAA Scitech 2022 Forum. AIAA Paper 2022-0122.
- SONG, M., SEÇKİN, S., SALEH, Y., ZIGUNOV, F., KUMAR, R. & ALVI, F.S. 2023 Optimization of microjet control for supersonic impinging jet using genetic algorithm. AIAA Aviation 2023 Forum. AIAA Paper 2023-3354.
- TAM, C.K.W. 1995 Supersonic jet noise. Annu. Rev. Fluid Mech. 27, 17-43.
- TAM, C.K.W. & AHUJA, K.K. 1990 Theoretical model of discrete tone generation by impinging jets. *J. Fluid Mech.* **214**, 67–87.
- TAM, C.K.W. & Hu, F.Q. 1989 On the three families of instability waves of high-speed jets. *J. Fluid Mech.* **201**, 447.
- TOWNE, A., CAVALIERI, A.V.G., JORDAN, P., COLONIUS, T., SCHMIDT, O., JAUNET, V. & BRÈS, G.A. 2017 Acoustic resonance in the potential core of subsonic jets. *J. Fluid Mech.* **825**, 1113–1152.
- TOWNE, A., SCHMIDT, O.T. & COLONIUS, T. 2018 Spectral proper orthogonal decomposition and its relationship to dynamic mode decomposition and resolvent analysis. *J. Fluid Mech.* **847**, 821–867.
- WEIGHTMAN, J.L., AMILI, O., HONNERY, D., EDGINGTON-MITCHELL, D. & SORIA, J. 2019 Nozzle external geometry as a boundary condition for the azimuthal mode selection in an impinging underexpanded jet. J. Fluid Mech. 862, 421–448.
- WYATT, L.A. 1958 Tests on the loss of vertical jet thrust due to ground effect on two simple vtol planforms, with particular reference to the short sc1 aircraft. Aero. Res. Counc. R&M 3313, 1–40.